Characterization of Precipitates in Steam Methane Reformer Tubes

by

Sakinah Binti Haris

Dissertation submitted in partial fulfillment of
the requirements for the
Bachelor of Engineering (Hons)
(Mechanical Engineering)

SEPTEMBER 2012

Universiti Teknologi PETRONAS
Bandar Seri Iskandar
31750 Tronoh
Perak Darul Ridzuan

CERTIFICATION OF APPROVAL

Characterization of Precipitates in Steam Methane Reformer Tubes

by

Sakinah Binti Haris

A project dissertation submitted to the
Mechanical Engineering Programme
Universiti Teknologi PETRONAS
In partial fulfillment of the requirement for the
BACHELOR OF ENGINEERING (Hons)
(MECHANICAL ENGINEERING)

Approved by,

_____

(Dr. Azmi Bin Abdul Wahab)

UNIVERSITI TEKNOLOGI PETRONAS
TRONOH, PERAK
September 2012

CERTIFICATION OF ORIGINALITY

This is to certify that I am responsible for the work submitted in this project, that the original work is my own except as specified in the references and acknowledgements, and that the original work contained herein have not been undertaken or done by unspecified sources or persons.

_____

SAKINAH BINTI HARIS

ABSTRACT

Reformer tubes are critical components in steam-methane reformers and they are exposed to severe conditions of high temperature and pressure of endothermic hydrogen reforming reaction. The elevated temperature condition induced the reformer tube material to experience creep damage. It is vital to extend the life of the reformer tube in order to reduce the maintenance cost. The prolonged heating also developed carbide precipitations in the reformer tube. In this work, a study has been conducted to characterize the precipitates in the steam-methane reformer tube. The precipitates were characterized in terms of type and size, and the characterizations were then related to the conditions of an ex-serviced reformer tube.

ACKNOWLEDGEMENT

At first, I would like to express my gratitude to Allah S.W.T that had made my final year project ran smoothly and end successfully. A greatest appreciation goes to Dr. Azmi Abdul Wahab, my final year project's supervisor for his teachings, guidance, supports and supervision towards completing my project. From such project, I have gained valuable knowledge and deepened my comprehension regarding the microstructure characterization and its behavior which I believe could be useful in my future application and contribution. A lot of explanation and support has been given by my supervisor to get through the hardest part of completing the project. In the hard times, I have learnt values to always be positive, patient, determine and persevere to achieve the goal. Also, special thanks to my family and colleagues for their moral support, inspiration and advice throughout the period. May all of you gain His Blessings and His Love.

TABLE OF CONTENTS

CERTIFICATION OF APPROVAL i

CERTIFICATION OF ORIGINALITY ii

ABSTRACT iii

ACKNOWLEDGEMENT iv

LIST OF FIGURES vii

LIST OF TABLES ix

CHAPTER 1: INTRODUCTION 1

1.1 Background of Study 1

1.2 Problem Statement 3

1.3 Objectives of Study 3

1.4 Scope of Study 3

CHAPTER 2: LITERATURE REVIEW 4

2.1 Steam Methane Reformer . . . 4

2.2 Steam Methane Reformer Tubes . . . 5

2.3 Carbide Precipitations in Reformer Tubes . 6

2.4 Characterization of Carbide Precipitates in Austenitic Stainless Steel 8

2.5 Quantitative Image Analysis . . . 13

CHAPTER 3: METHODOLOGY 16

3.1 Project Framework 16

3.2 Imaging Tools 17

3.3 Preliminary Research 18

3.4 Collection and Organization of Data . . 18

3.5 Data Processing 19

3.5.1 Cropping image 19
3.5.2 Highlighting precipitates features . 20
3.6 Analyze Data 21
3.6.1 Area threshold 21
3.6.2 Area measurement . . . 23
3.6.3 Three Dimensional (3D) reconstruction and visualization 25
CHAPTER 4: RESULT AND DISCUSSION . . . 27
4.1 Result 27
4.2 Effect of different service temperature on the precipitation formation 27
4.3 Service condition of the sample XC and XH . 32
CHAPTER 5: CONCLUSION AND RECOMMENDATION . 37
5.1 Conclusion 37
5.2 Recommendation 38
REFERENCES 39

LIST OF FIGURES

Figure 1.1	The effect of exceeding the design temperature on the expected life of HK-40 alloy reformer furnace tubes. .	2
Figure 2.1	Scheme of a hydrogen production system comprising a steam-methane reformer	5
Figure 2.2	Schematic view of a top fired reformer furnace . .	6
Figure 2.3	Microstructure of as-cast and after annealing alloys . .	9
Figure 2.4	Multiphase aggregated carbides on the grain boundaries after the annealing and results of quantitative microprobe analysis of the precipitates and the matrix (%). . . .	10
Figure 2.5	Backscatter electron (BSE) image of ex-service reformer tube and the corresponding EDS spectra of precipitates *A*, *B*, and *C*	12
Figure 2.6	XRD Spectrum of reformer tube precipitates. $M_{23}C_6$, NbC and TiC peaks are indicated	12
Figure 2.7	Three dimensional reconstruction can be obtained by systematic thinning of specimen.	15
Figure 3.1	The flow chart of project methodology . . .	16
Figure 3.2	The NIH ImageJ user window.	18
Figure 3.3	Process of cropping image from the raw stack images. a) 664 x 470 pixels rectangular selection of stack images b) with 50% zoom. b) Cropped image viewed in 100% zoom.	20
Figure 3.4	Image processing. a) Type of precipitates was determined. b) Highlighted $Cr_{23}C_6$ precipitates features. c) Highlighted NbC precipitates features. d) No presence of TiC to be highlighted. . . .	21
Figure 3.5	Command windows to adjust image with color threshold. .	22
Figure 3.6	Particle regions threshold for the first layer of sample K0; $Cr_{23}C_{6.}$	23
Figure 3.7	Re-scaling the measurement unit from pixels into µm.	23
Figure 3.8	Command to analyze particles threshold. . . .	24
Figure 3.9	Result presentation of analyzed particle threshold; masks of particles, table of results, and result summary. . .	24

Figure 3.10 Microsoft Excel spreadsheet used to tabulate the entire stacks of analyzed particles. 25
Figure 3.11 The masks images of sample K0 were re-stack and saved in different TIFF file. 26
Figure 3.12 The volume viewer showing the distributions of $Cr_{23}C_6$ of sample K0 in isometric view. 26
Figure 4.1 Graph of mean volume of precipitate against the service temperature. 28
Figure 4.2 Optical image of Sample K1 at 200X magnification.. . 29
Figure 4.3 Optical image of Sample K2 at 200X magnification.. . 30
Figure 4.4 Optical image of Sample K3 at 200X magnification.. . 30
Figure 4.5 Optical image of Sample K0 at 200X magnification.. . 31
Figure 4.6 The mean volume of Chromium Carbide precipitates against the service temperature 32
Figure 4.7 The mean volume of Niobium Carbide precipitates against the service temperature 33
Figure 4.8 The mean volume of Titanium Carbide precipitates against the service temperature 33
Figure 4.9 The linear regression of mean volume of $Cr_{23}C_6$ with the operating temperature 35
Figure 4.10 The linear regression of mean volume of NbC with the operating temperature 35
Figure 4.11 The linear regression of mean volume of TiC with the operating temperature 36

LIST OF TABLES

Table 2.1	Nominal Composition of Principal Alloys Used for Tubular Tubular	7
Table 2.2	Comparison of selected properties of human and computerized vision system when applied in metallography . .	13
Table 3.1	Detail service condition of the samples . . .	18
Table 3.2	Chemical Composition of Schmidt + Clemens CA4852 micro alloy material	19
Table 4.1	Data tabulation of average particle size to the service temperature	27
Table 4.2	XH and XC tabulated data	34
Table 4.3	Table for calculated temperature based on linear equations produced in graphs	34

CHAPTER 1

INTRODUCTION

1.1 Background of Study

Reformer furnaces are used in petrochemical industry to produce hydrogen, carbon monoxide and carbon dioxide. More recently, with the increase of hydrogen gas demand, reformer furnaces are widely used for the large scale production of hydrogen gas. Reforming process is also well known for its economical way of production [1]. With the catalytic reactions that occur, the reactants – hydrocarbons and steam are converted into hydrogen and carbon dioxide [2]. The following are the general reactions of the process in the reformer furnaces.

$$C_nH_m + nH_2O \longrightarrow nCO + (m/2 + n)\,H_2 \qquad (1)$$

$$CO + H_2O \longrightarrow CO_2 + H_2 \qquad (2)$$

Most reformer furnaces undergo Steam-Methane Reforming (SMR). However, other C_nH_m, hydrocarbons such as ethanol, propane or even gasoline are also used in reforming process of hydrogen [3]. The above endothermic reaction is conducted in high temperature of a steam reformer furnace with temperature exceeding 1073K for the reaction to take place. The steam reformer furnace contains numerous vertically mounted tubes filled with catalyst in which they are continuously heated to achieve the required temperature. Thus, the critical components of a reformer furnace are the reformer tubes themselves due to the severe heat exposure during the service [2].

Steam reforming tubes are usually made of centrifugally cast austenitic stainless steel [4]. It is designed with normal life of 100,000 hours, however, in real service conditions the life varies depending on the service condition and the characteristic of materials used [5]. Upon the severe heating of the reformer tube, the microstructure of

the cast stainless steel will change substantially resulting in a change in mechanical properties. The microstructural changes however, could be used to determine the actual wall temperature and also other mechanical attributes of the material itself [6].

Research has confirmed that, the most important damage mechanism leading to the failure of the reformer tube is creep, and it is shown in Figure 1.1, the effect of increased local temperature could cause a dramatic reduction in life. From the figure, it is shown that the further the difference between average temperature from its base design temperature, the lesser the percentage of expected tube life of an alloy [7]. Most of the existing study illuminates the variations of microstructure and mechanical properties of the tubes during the operation along with time and usually relates in determination of remaining lifetime of the tubes.

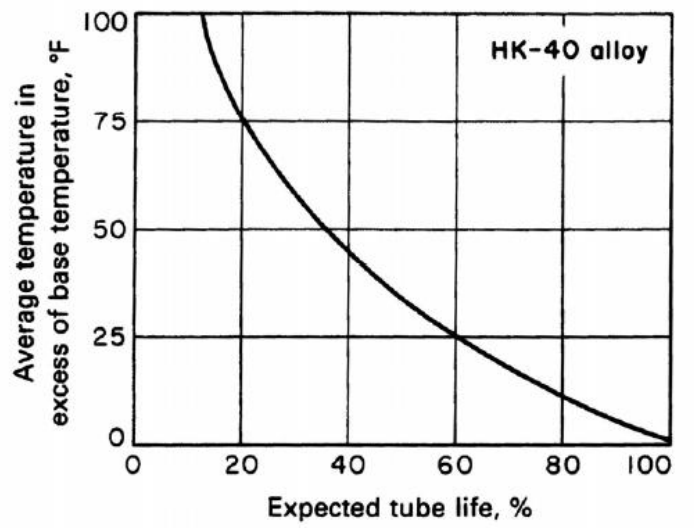

Figure 1.1: The effect of exceeding the design temperature on the expected life of HK-40 alloy reformer furnace tubes [7].

However, research has also found that, the presence of secondary precipitates as an effect of the heating inside the reformer tubes may contribute to creep strengthening of the material and may cause tube failure [8]. Therefore, the purpose of this project was to investigate the relationship between the precipitations in reformer tube with the service condition.

1.2 Problem Statement

Reformer tubes are the critical components of a reformer furnace due to severe heat exposure during service. The material that is generally used for reformer tubes is a type of special cast alloys with increased creep strength, greater resistance to overheat, and longer tube service life [8]. The heating process during the operationwould change the material microstructure such thatcarbide precipitations form at the interdendritic region [9]. It would be of great intent to relate the characterization of these precipitates to the service condition of the material.

1.3 Objectives of Study

The main objectives of this project are:

I. To characterize themicrostructure of the precipitate that form in the ex-service reformer tube by using metallography and microscopy techniques.
II. To correlate between the microstructural features of precipitates to the service condition of the tube.

1.4 Scope of Study

In this project, all the samples of ex-serviced reformer tubes were obtained from MethanexKitimat Plant, Canada. The reformer tube material is Schmidt + Clemens CA4852 micro alloy from Spain. The samples data are given the nomenclature and operating conditions section. Total five samples were analyzed which were randomly sectioned out at different length of the same reformer tube. Three of them were provided with operating conditions information while the remaining two were only stated to be in overheated service condition and at normal service condition respectively.

Characterization process will involve analysis of optical microscopy data obtained from the metallographic sample prepared. Characterization of precipitates will be limited to Chromium Carbide ($Cr_{23}C_6$), Niobium Carbide (NbC) and Titanium Carbide (TiC) precipitates only. The amount and size of the precipitates will be related to the service conditions experienced by the tube.

CHAPTER 2

LITERATURE REVIEW

2.1 Steam Methane Reformer

In petrochemical industry, Steam-Methane Reforming (SMR) Process has been extensively used in production of hydrogen from fossil fuels, in which the methane reacts with steam to produce a mixture of hydrogen (H_2), carbon dioxide (CO_2) and carbon monoxide (CO) [10]. A mixture of CO_2 and H_2 then is used to produce chemical products with high added values such as hydrocarbons and oxygenated compound. It is a very energy intensive process due to highly endothermic reaction which is well suited for processes requiring a H_2-rich feed like ammonia synthesis and petroleum refining process [9].

Figure 2.1 briefly describe the flow of hydrogen production process comprising steam-methane reforming process inside the reformer. The steam reformer is where the high-energy endothermic reaction of reforming process takes place. Firstly, the fuel preparation section takes place to cleanse the feed water and desulphurize the methane gas before they are mixed into the reformer furnace. In the second section, there are two main processes that occur; steam-methane reforming and water-gas shift reaction.

1. Steam-methane reforming

   In steam-methane reforming methane reacts with high temperature steam (970 – 1100K) at 3.5MPa in the presence of a catalyst to produce CO and H_2. Steam-methane reforming is endothermic in which heat must be supplied for the reaction to occur [11].

$$CH_4 + H_2O \rightarrow CO + 3H_2 \qquad \Delta H°298 = +\ 241\ \text{kJ/mol} \qquad (3)$$

2. Water-gas shift reaction

   In this phase, exothermic reaction of CO with H_2O (steam) is then carried out to produce H_2 at 470 – 820K [3]. Conventionally, the process is performed in multi-tubular fixed-bed reactors in the presence of a metal catalyst [12].

$$CO + H_2O \rightarrow CO_2 + H_2 \qquad \Delta H°298 = -41.1 \text{ kJ/mol} \qquad (4)$$

In the purification section, pressure swing adsorption is commonly used to remove CO_2, water, methane and CO from the off gas leaving essentially the pure H_2 [11]. The unwanted gases would then be recycled to the reformer through off-gas vessel.

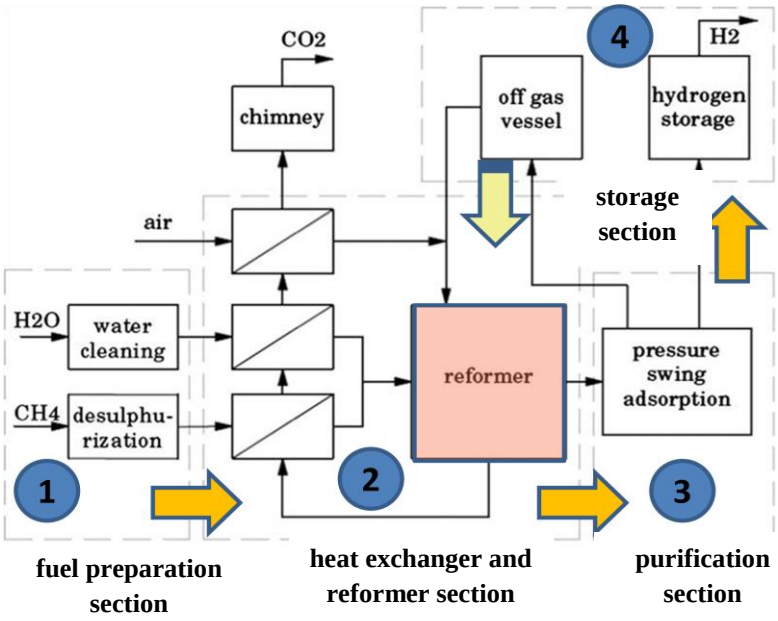

Figure 2.1: Scheme of a hydrogen production system comprising a steam-methane reformer. [1]

2.2 Steam-Methane Reformer Tubes

The design of steam-methane reformer tubes has greatly improved over the past 30 years. The alloys and manufacturing process development has contributed to meet the severe requirements of the reformer tubes, which are operating in the radiation zone and in the hot reaction gas outlet. The use of catalyst such as Nickel (Ni) also provide lower temperature reactions thus aiding to equalize the need of increase temperature

and pressure to achieve further increases in production and reformer furnace efficiency [7].

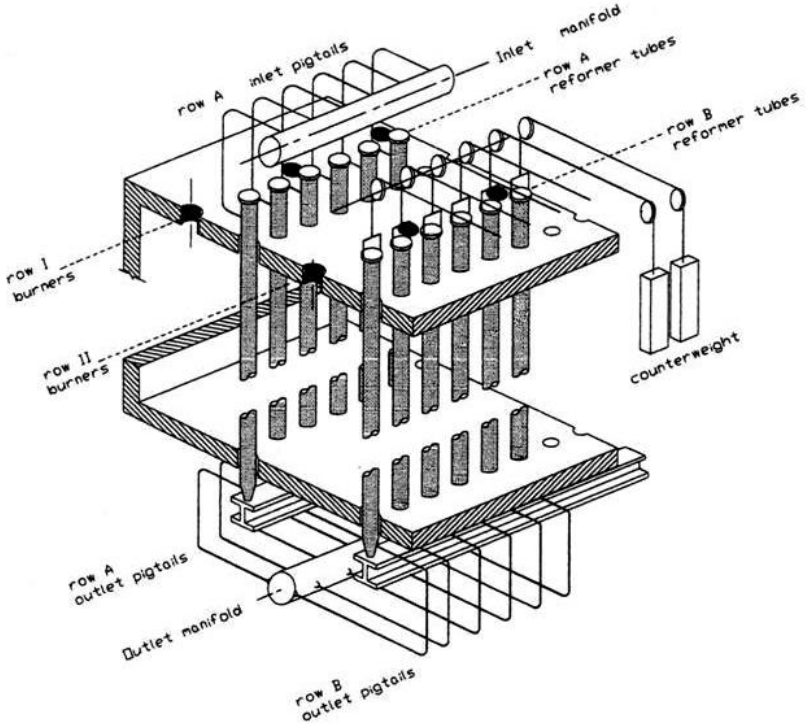

Figure 2.2: Schematic view of a top fired reformer furnace [7].

A steam reformer is made up of catalyst-filled reformer tubes arrays arranged in the form of two vertical walls. The number of columns varies between 15 and 200; depend on the number and size of the walls. Most of the reformer furnaces are of the top-fired type at which the burners are dispersed rows on both side of columns. Charge will be given through the inlet pigtails above the roof of radiation chamber and the reformer tubes column is suspended with use of counterweights. The producing gas will then leave the column through the outlet pigtails connecting to outlet manifold [7].

2.3 Carbide Precipitation in Reformer Tubes

On the basis of API 530, the design of nominal life of a reformer tube should be 100,000 hours however it depends on the actual operating conditions and characteristic of the particular tube material. Owing to the severe operating conditions, reformer tubes are typically made of ACI HK40 (0.4 wt%C – 25 wt%Cr –

20 wt%Ni) and ACI HP40 (0.4 wt%C – 25 wt%Cr – 35 wt%Ni) [4]. The dimensions of the reformer tubes manufactured vary between 10 and 15m in height, 100 to 200mm diameter, and 10 to 25 mm wall thickness [4].

Since early 80s, modern alloys such as the HP types have been made available in which it contributes to strength and corrosion resistance at high temperature. Table 2.1 below presents the nominal composition of principal alloys used for reformer tubes manufactured by Schmidt + Clemens (S+C) & Co. KG [9].

Table 2.1: Nominal Composition of Principal Alloys Used for Tubular Reformers [9].

Nominal Composition of Principal Alloys Used for Tubular Reformers						
Common name (ACI)	**C %**	**Cr %**	**Ni %**	**Nb %**	**Other**	**S+C Centralloy® grade**
HP-Nb	0.40	25.0	35.0	1.0	–	G 4852
HP-Micro-alloy	0.45	25.0	35.0	1.0	Micro-alloy additions	G 4852 Micro
HP- Micro-alloy	0.45	25.0	35,0	1.0	Micro-alloy additions	G 4852 Micro R

As presented by Schmidt + Clemens (S+C) & Co. KG, during the service of reformer tube, a significant number of full thermal and pressure cycles caused by plant start-ups and shut-downs happens throughout the process. This condition can be very damaging and could accelerate creep cracking. For reformer tubes, which are working under severe condition, centrifugally cast material, are mostly favored [9].

During the metal casting of the tube material, primary eutectic-like carbide network formation plays important role in preventing grain boundary sliding [13]. However, at the early stages of SMR process, precipitation of carbides occurs in reformer tubes. This would reduce the strength and cause embrittlement of materials due to coalescence and coarsening of carbides. Further degradation could lead to creep damage, micro cracking and final propagation of macro-cracks [5]. The carbide formation consists of austenitic dendrites surrounded by eutectic carbides in the interdendritic region. This carbide formation is also known as secondary precipitation.

Studies have been done proving that better creep properties have been attributed to the morphological modification and the presence of more stable phases during the long-

term service. The recent modification of adding niobium-plus-titanium has promoted the fragmentation of the as-cast microstructure and partially replaces the chromium carbide into more stable ones. It is in the form of a fine-distribution of cube-shaped chromium carbides that it should act to restrict the motion of dislocations [13]. This proves that alloys do rely upon creep strengthening by the formation of more stable carbides in the microstructure especially during a long-term high temperature service [9].

2.4 Characterization of Carbide Precipitates in Austenitic Stainless Steel.

Based on the microstructure study of the as-cast and annealed austenitic steels, findings have shown that in the as-cast state, the microstructure comprise of austenitic matrix and primary precipitates of carbide which are present at the boundaries of grains and in the interdendritic areas.

Figure 2.3 shows the comparison of microstructure before and after the alloys were annealed. Alloys 1 and 2 above show the effect of titanium and niobium addition, respectively. It is proven that annealing significantly changed the microstructure of the alloys. Also alloys 1 and 2 show changes at and around the boundaries of austenite grains with large amounts of fine secondary precipitates at the matrix interfaces.

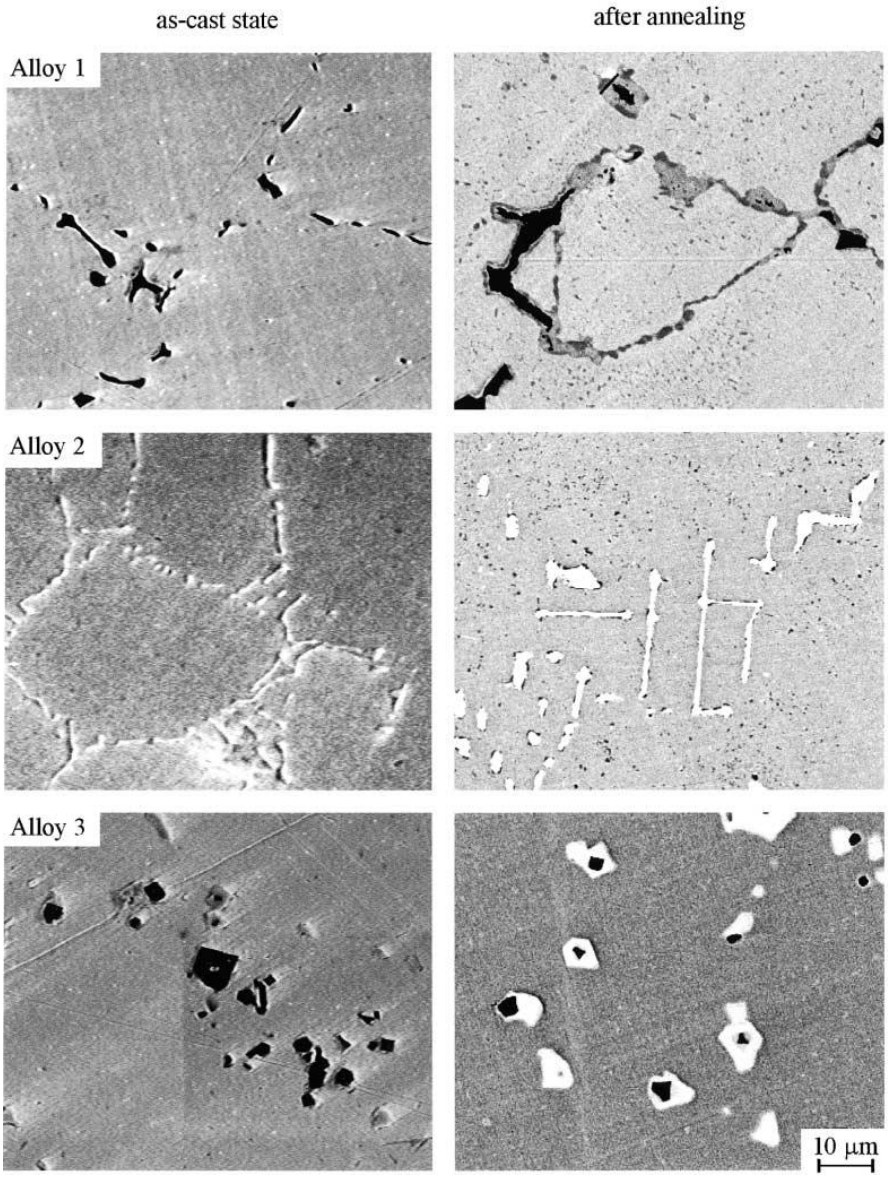

Figure 2.3: Microstructure of as-cast and after annealing alloys. [14]

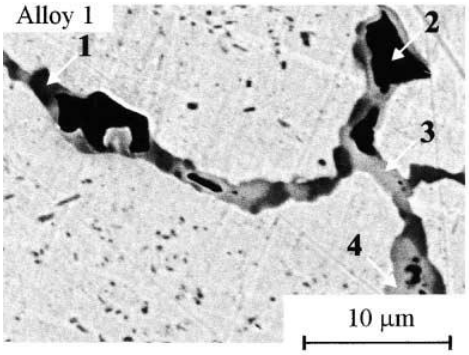

	Si	Fe	Cr	Ni	Ti
1	0.57	15.1	71.9	9.3	3.13
2	0.70	3.4	3.9	6.6	85.4
3	10.6	7.7	4.3	51.2	26.2
4	10.4	5.8	9.7	48.4	25.7
matrix	2.27	49.1	19.2	29.2	0.23

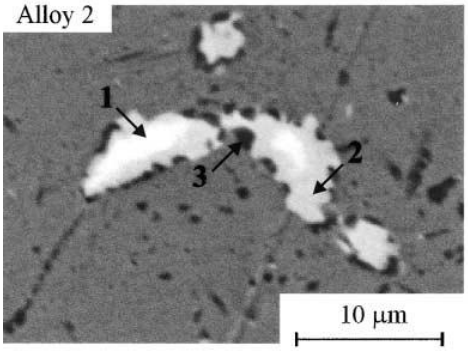

	Si	Fe	Cr	Ni	Nb
1	0.45	1.1	1.6	2.15	94.7
2	8.0	6.3	2.6	35.9	47.2
3	0.36	15.0	76.5	6.44	1.7
matrix	2.10	47.9	19.2	30.8	—

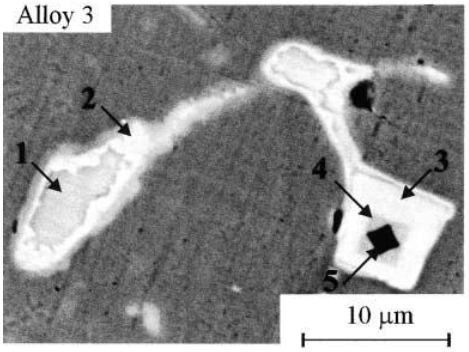

	Si	Fe	Cr	Ni	Nb	Ti
1	—	0.6	0.7	0.7	71.7	26.3
2	7.3	4.2	1.1	33.3	40.0	14.1
3	—	0.7	0.4	0.3	74.5	24.1
4	—	0.6	0.5	0.4	68.8	29.7
5	—	0.6	0.5	0.4	33.6	64.9
matrix	1.6	48.3	20.0	29.6	—	0.5

Figure 2.4: Multiphase aggregated carbides on the grain boundaries after the annealing and results of quantitative microprobe analysis of the precipitates and the matrix (%) [14].

Figure 2.4 above shows the confirmed microstructure of carbide elements in the alloys tested. The microanalyses were performed by using microprobe analysis. The results are concluded as follows [14]:

Alloy 1: Precipitate 1 is chromium carbide of $M_{23}C_6$type; precipitate 2 is TiC carbide while the areas 3 and 4 are rich in nickel, silicon and titanium. It is proven that not all titanium is used in formation of the TiC during solidification process.

Alloy 2: Precipitate 1 is probably NbC carbide; precipitate 3 is chromium carbide $M_{23}C_6$ type. The chemical analysis in area 2 indicates rich of silicon, nickel, and niobium.

Alloy 3: Precipitates 1 and 3 are NbC carbides alloyed with titanium, precipitate 5 is TiC carbide alloyed with Nb. The area 4 is probably a secondary solution of both Ti and Nb carbide. TiC –NbC complex and the NbC carbides are denoted by number 2. It was rich in silicon, nickel, niobium and titanium, Pheses rich in silicon, nickel and niobium in austenitic alloys reported earlier in other findings [15,16], the phase has been named "G" phase and the formula of $Nb_6Ni_{16}Si_7$ has been attributed.

In a previous research identification of precipitates that form in the same reformer tube originated from Methanex Kitimat Plant, Canada has been made. Precipitates A and B as labeled in Figure 2.5(a), appeared as light blue and grey respectively, and were usually found along the grain boundaries. From the EDS result shown in Figure 2.5(b), precipitates A show the highest content of chromium elements and it was confirmed in a XRD method that the precipitate A is $Cr_{23}C_6$ as illustrated in Figure 2.6. The EDS confirmed precipitates B and C to be NbC and TiC respectively as shown in Figure 2.5(c) and (d). Precipitate C appeared as orange-brown and usually resided intragranularly. In the sample, there is also presence of void, which appeared next to precipitate A [3].

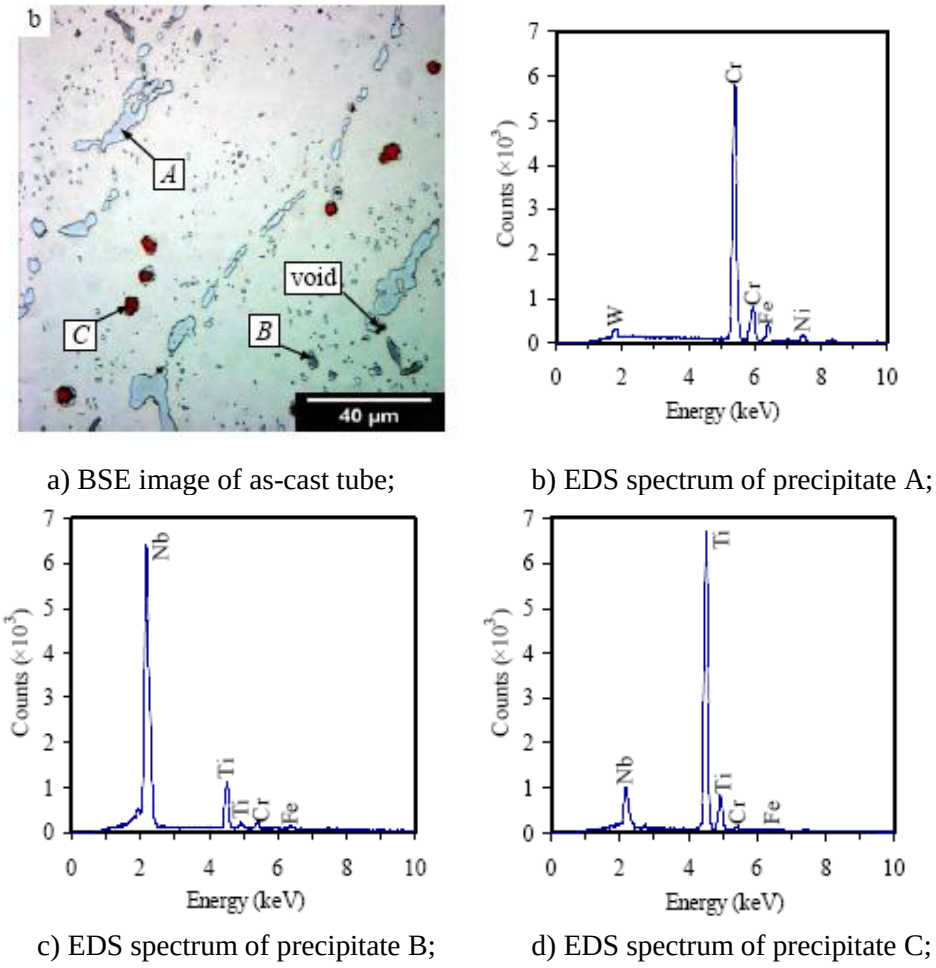

Figure 2.5: Backscatter electron (BSE) image of ex-service reformer tube and the corresponding EDS spectra of precipitates *A*, *B*, and *C* [3].

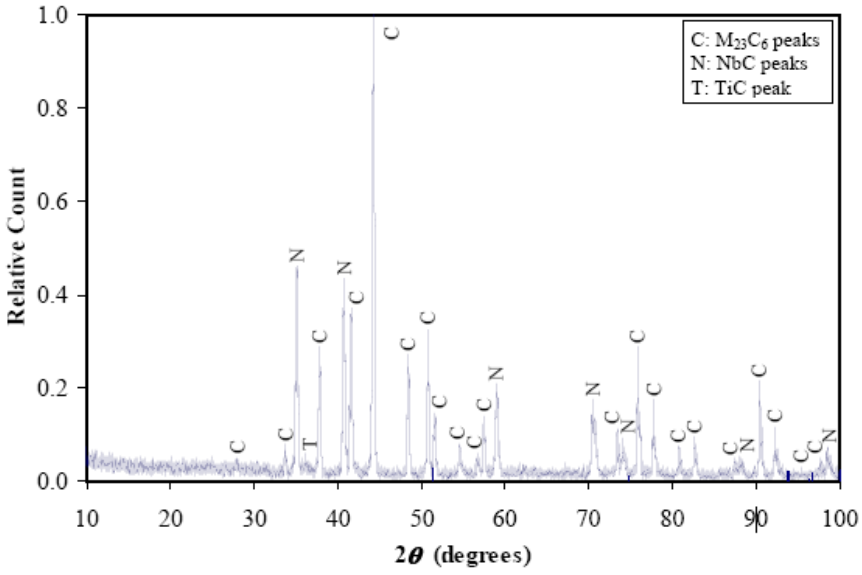

Figure 2.6: XRD Spectrum of reformer tube precipitates. $M_{23}C_6$, NbC and TiC peaks are indicated [3].

2.5 Quantitative Image Analysis.

In material characterization, quantitative image analysis is developed to extract meaningful information from microstructure images captured. It can be assessed by human manually or automatically conducted by machine that has been allowed for the construction of personal-computer-based digital image analyzers. Nevertheless, this enormous progress of the machine has been implemented on a limited scale due to introduction of user-friendly, icon-based software that can be applied on any computer device. People are afraid of using computerized tools in metallographic laboratory and declare that the machine would never do as good and thorough analysis as an experienced metallographic practitioner. The comparison between the traditional and computer-aided image analysis based on certain properties is shown in Table 2.2.

Table 2.2: Comparison of selected properties of human and computerized vision system when applied in metallography [15].

Analyzed feature or property	Traditional analysis using human visual system	Computer-aided image analysis
Human fatigue after prolonged work	Very sensitive	Insensitive
Sensitivity towards illusion	Very sensitive	Insensitive
Required image quality	Medium quality acceptable for quantitative analysis	Highest quality standard
Repeatability of results	Low	Full repeatability in totally automatic analysis
Reproducibility of results	Low	Full reproducibility
Cost of analysis	Low for single specimen; rapid growth with increasing number of specimens	High for single specimen; significant drop per unit as number of routine investigations increases
Quantitative assessment of microstructure	Time-consuming; some parameters cannot be evaluated	Can be very good
Qualitative assessment of microstructure	Can be very good	Poor and difficult
Speed of analysis	Slow, especially in quantitative analysis	Fast, especially for on-line analysis
Operator experience	Significant effect on the results	Negligible effect for routine tasks; very important during implementation of the system

Image is a representation of an object produced by lens or mirror system. The image is a data set, stored in a computer memory or in a digital file that can be displayed on screen or printed for human observation. The elementary unit of a digital image is called pixel. When an image is displayed in a computer monitor, it is a mosaic of pixels. The location of each pixel is defined by the image format (Tagged Image File Format or TIFF, BMP, Joint Photographic Expert Group or JPEG, etc.). The body of the digital file contains information concerning pixel intensity or color [15].

Image processing is part of image analysis. It is a process of data transformation in which the initial data set is an image or a collection of images and the final, resulting data set is also an image or a collection of image. Image processing also can be called digital imaging, as is done within this volume. The aim of image processing is to highlight the features under investigation or to suppress the unwanted features. The process of image acquisition is usually interpreted as the introductory part of image processing. Image processing, in image analysis – the computer modification of a digitized image on a pixel-by-pixel basis is to emphasize certain aspects of the image. The final step of image analysis can be in various characters such as characterizing the grain size [15].

Digital measurement are the core of quantitative image analysis as to determine the size distribution. According to ASTM, estimation of the mean object section area can be calculated using the formula below,

$$\bar{a} = \frac{A_A}{N_A} \tag{5}$$

where$\bar{a}$ is the mean object area, $A_A$is the area fraction of the objects analyzed, and N_A denotes the number of objects per unit section area.

To characterize sructural parameters of any microstructure, they are four characters that are necessary to describe its properties which are amount, size, shape and spatial distribution of all the phases. However of all, distribution is the most difficult to quantify. Any material built of two or more phases is non-homogenous. When it is oberseved at very high magnification only the phases can be distinguished clearly. On

the other hand, when the microstructure is observed by human eye, it can seems to be homogenous. Therefore, the result of homogeneity quantification only applicable at high magnification. This situation can be improvised by using three-dimensional (3-D) images. The oldest technique for obtaining 3D data is to prepare a series of polished sections with a systematic shift in direction perpendicular in z-direction. There are some drawbacks in such method where it is practically impossible to ensure same step in z-direction and the resolution in this direction significantly lower than the section plane. Despite of these drawbacks, it is allowed for evaluation of real 3D shapes of grains [15].

From this systematic thinning of the specimen, the subsequent 3-D reconstruction can provide real shape and arrangement of features that are not available in any other methods. In contrast, image analysis packages or software equipped with 3-D analysis tools allow for filtering, binarization (two form 2 values of pixel) and measurement similar to those used in 2-D image analysis. Unfortunately, such ability requires huge computing power and computer memory to process the data. There is a software that could meet such requirements namely NIH ImageJ application software. It is known as the fastest image analyzer packages written in JAVA which is user-friendly and are now used worldwide. It is significance to do 3-D analysis as it offers the ability to obtain real, volumetric distribution of some features in the analyzed microstructure. Nevertheless, this 3-D has its own limitation that it is practically impossible to detect grain boundaries. Therefore, this techniques is suitable for assesment of porosity and homogeneity of phases in a microstructure. Figure 2.7 illustrates the 3-D reconstruction from the systematic thinning of specimen [15].

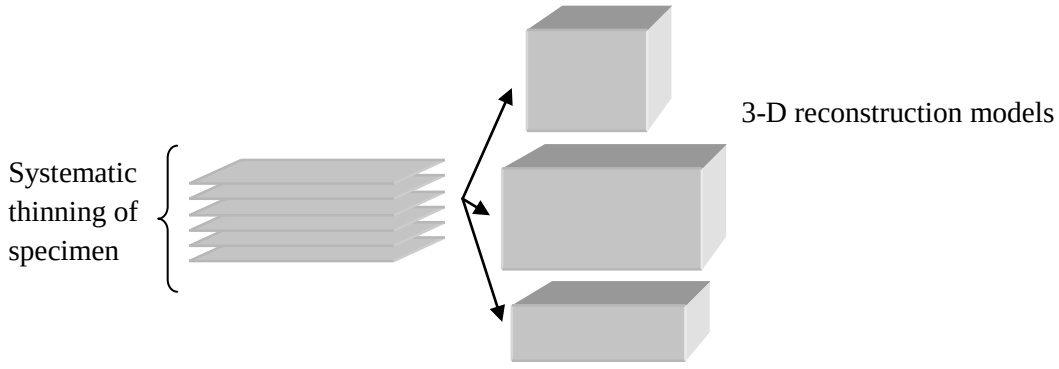

Figure 2.7: Three dimensional reconstruction can be obtained by systematic thinning of specimen.

CHAPTER 3

METHODOLOGY

3.1 Project Framework

The characterization of precipitates in this project has been conducted based on data obtained from prepared metallographic samples. Figure 3.1 shown below is the general step of conducting the project.

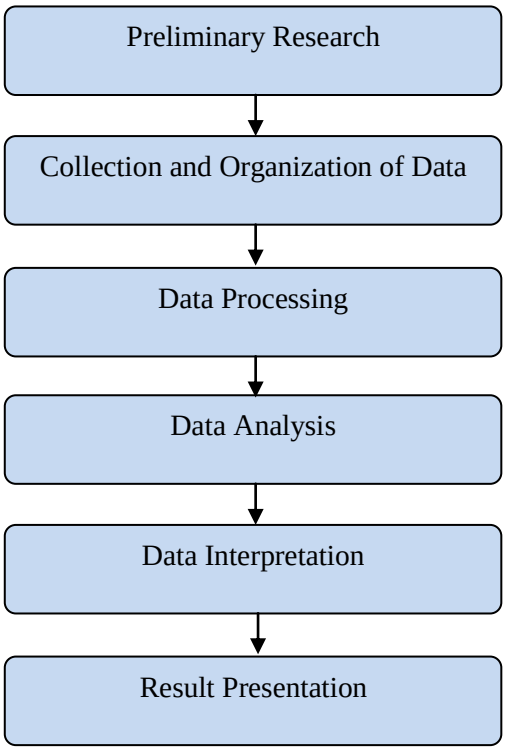

Figure 3.1: The flow chart of project methodology.

Samples for this work have been previously prepared metallographically. Optical images of the microstructure had been obtained at various location of the reformer tube. This project began with data organization to arrange the images according to their respective group samples. Next, the data have been processed by identifying the

respective precipitates from the images. The sizes of precipitates for each of the samples were analyzed by means of area measurement and 3-D reconstruction. All the samples have undergone same process. Finally, the result obtained were plotted on the graph for further interpretation and comparison between the known service condition samples with the unknown service condition to locate and determine the service condition experienced by the samples.

3.2 Imaging Tools

NIH ImageJ software was used throughout the image analysis. NIH ImageJ is an open-source software that their Java source codes are freely available in public domain and no license is required. Since it is written in Java, it allows running on Linux, Mac OS X and Windows, in both 32-bit and 64-bit modes. It has large and knowledgeable worldwide user community. It is the world's fastest pure Java image processing program that it can filter a 2048 x 2048 image in 0.1 seconds, about 40 million pixels per second. It can be opened and saved in all supported data types 8-bit grayscale or indexed color, 16-bit unsigned integer, 32-bit floating point and RGB as TIFF or as raw data. Other file formats are GIF, JPEG, BMP, PNG, PGM, FITS and ASCII. The zooming tools (1:32 to 32:1) are provided and all analysis and processing functions are able to work at any magnification factor [16].

Selections can be made by creating rectangular, elliptical or irregular area selection. To make irregular area selection, lines and point selection is created. Next selection is edited and automatically created using the wand tool. Drawing, filling, filtering or measuring of selection can be easily conducted through the program. For image enhancement, this software supports smoothing, sharpening, edge detection, median filtering and thresholding on both 8-bit grayscale and RGB color images. It is also can interactively adjust brightness and contrast of 8, 16, and 32-bit images. Other functions such as geometric operations, image analysis, image editing, and color processing are also featured in this ImageJ software. For geometric operations, the image can be cropped, scaled, resized and rotated. It can perform image analysis such as measure area, mean, standard deviation, min and max of selection image. It also uses real world measurement such as SI units. To cut, copy or paste images or selections by using AND, OR, XOR or "Blend" modes. It provides display a "stack"

of related images in a single window. The process applies to the entire stack using a single command [16].

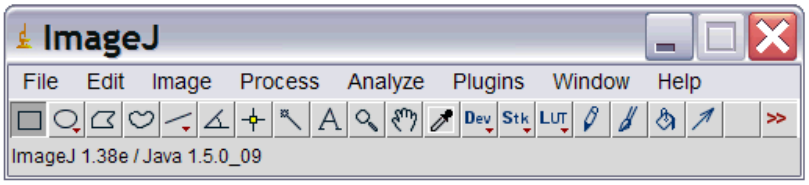

Figure 3.2: The NIH ImageJ user window [16].

3.3 Preliminary Research

Before conducting the experimental work, background of Steam-Methane Reformers were studied. The sources of information were obtained from articles, textbooks, journals and company websites. It is important to understand the operation of steam-methane reformer to relate the operation principles with carbide precipitations. At this stage the theory of precipitates formation due to annealing process also has been reviewed as well as characterization techniques done through researches.

3.4 Collection and Organization of Data

There are six data samples sectioned out from the same type of reformer tube used in this project work. Three of them, sample K1, K2 and K3 were all taken randomly with various operational conditions of their temperature and pressure in service as shown in Table 3.1 below while the remaining two samples were only known for its general serviced temperature under overheated or normal temperature. Sample K0 is the as-cast sample.

Table 3.1: Detail serviced condition of the samples.

Sample	Service hours (hr)	Distance from top flange (m)	Temperature in service (°C)	Pressure in service (MPa)
K0	N/A	N/A	N/A	N/A
K1	90,000	12.5	878 – 888	1.82
K2	90,000	9.9	867 – 886	1.91
K3	90,000	2.4	775 – 848	2.16
XH	90,000	Unknown	Overheated temperature	Unknown
XC	90,000	Unknown	Normal temperature	Unknown

The chemical compositions of the Schmidt + Clemens CA4852 micro alloy reformer tube samples were listed in Table 3.2.

Table 3.2: Chemical Composition of Schmidt + Clemens CA4852 micro alloy material [17].

Chemical Composition	**C**	**Si**	**Mn**	**Cr**	**Ni**	**Nb**	**Ti**	**Fe**
Mass percentage	0.45	1.50	1.00	25.0	35.0	1.50	Additions	Balance

The data obtained was in the form of TIFF (Tagged Image File Format) files of optical microscopy images with 200X magnification and had been aligned previously. Each sample was provided with 50 images of its consecutive layers after polishing with approximate depth of 0.5μm each. By using the ImageJ software the images were orderly stacked and was saved as one TIFF file. The same procedure was done to the other four samples. The 'image stack' allows the images to be displayed and processed through the same window. For every consecutive layer, the changes of microstructure are approximately 0.5μm depth.

3.5 Data Processing

Data processing is the image processing stage in which the initial images were transformed into other type of image. The aim of this image processing is to highlight the image of respective precipitates; Chromium Carbide, Niobium Carbide and Titanium Carbide. Each stacked image sample has undergone three modification processes and the precipitates were selected traditionally with reference from preliminary research regarding the precipitates features. The selected regions were the coarse precipitates and were kept constant for the whole layers to reduce errors during the analysis.

3.5.1 Cropping image

The raw 'image stack' were then cropped randomly into 664 x 470 pixels image. It is randomly cropped at the region with well-defined shape of precipitates as well as no external disturbance such the superimposed indentations image. Figure 3.3 shows the image is cropped from raw images at 50% zoom and after that appeared in 100% zoom.

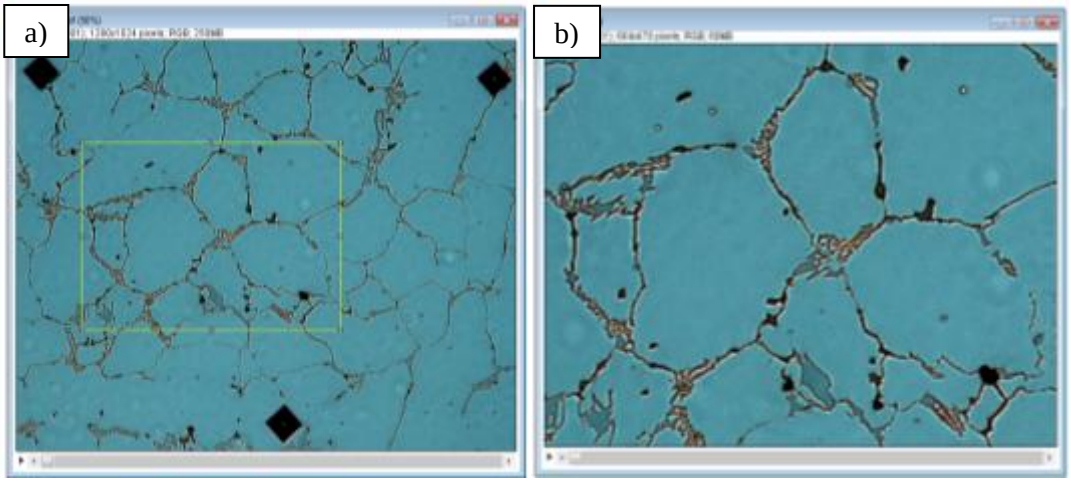

Figure 3.3: Process of cropping image from the raw stack images. a) 664 x 470 pixels rectangular selection of stack images with 50% zoom. b) Cropped image viewed in 100% zoom.

3.5.2 Highlighting precipitates features

Before the image could be analyze with area measurement and 3-D reconstruction, the image stacks were processed in which the features of interest were highlighted. The process is conducted by using NIH ImageJ paint tools where the background colors were picked to erase the non-interest features. The same highlighting process was done to the entire series of images to generate a new stack of images with feature of interest only.

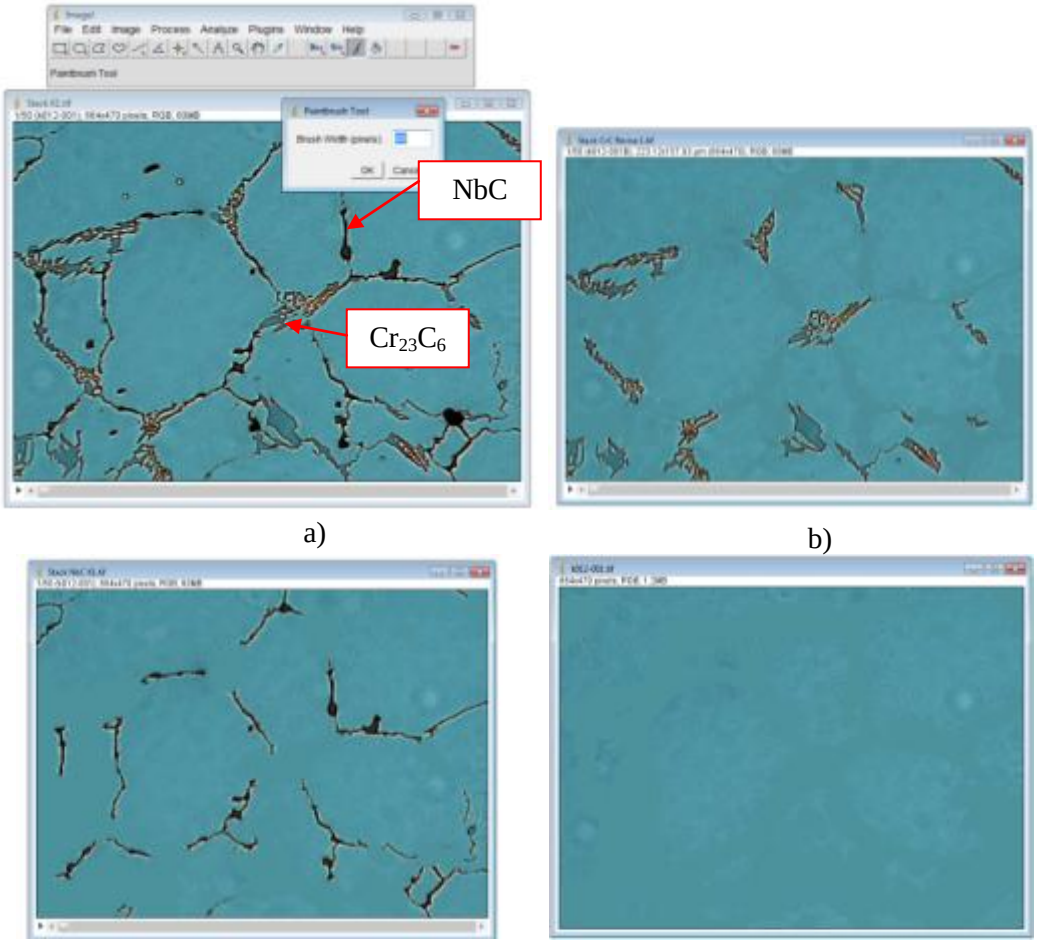

Figure 3.4: Image processing for sample K0. a) Type of precipitates were determined. b) Highlighted $Cr_{23}C_6$ precipitates features. c) Highlighted NbC precipitates features. d) No presence of TiC highlighted.

3.6 Analyzing Data

Data analysis has been done on basis of quantitative image analysis. The sizes of precipitates from the images captured were measured and the resulting size is defined by the estimated volume of precipitates in the samples. The mean area of stacked images is measured and each of the images in the stack would undergo same process.

3.6.1 Area threshold

After the precipitates features of interest have been processed, the selected region of precipitates would undergo color thresholding since the automatic particle analysis requires the image to be a 'binary' image. The software needs to know exactly where the edges are to perform morphology measurements. A 'threshold' range was set and

pixels in the image whose value lies in this range are converted to red as requested while pixels with values outside this range are converted to white.

The thresholding process is a bit more complicated as each of hue, saturation and brightness channels requires different threshold range as described shown Figure 3.6. Manual thresholding requires human interpretation on which area were being thresholded. Therefore to improve the quality of thresholding, the images were unstack and thresholded individually otherwise the calculated threshold of the currently displayed slice will be used for all slices. The images should also been re-scaled to get the measurement in unit of micrometer as in Figure 3.7. It would be useful in area measurement in the next stage of image analysis.

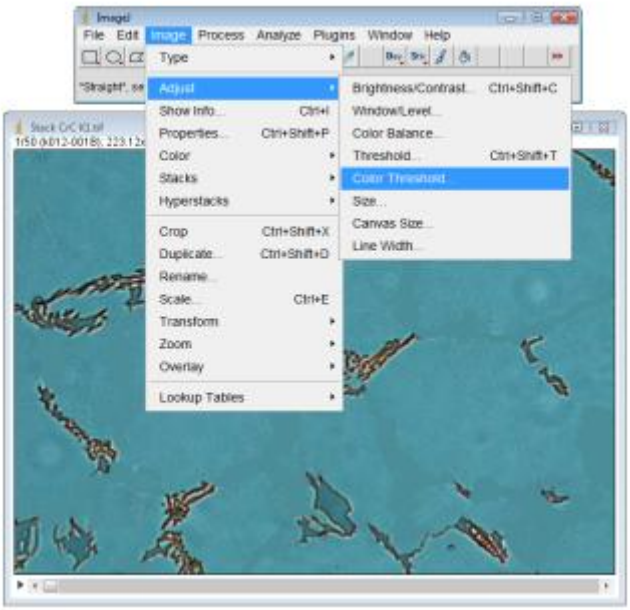

Figure 3.5: Command windows to adjust image with color threshold.

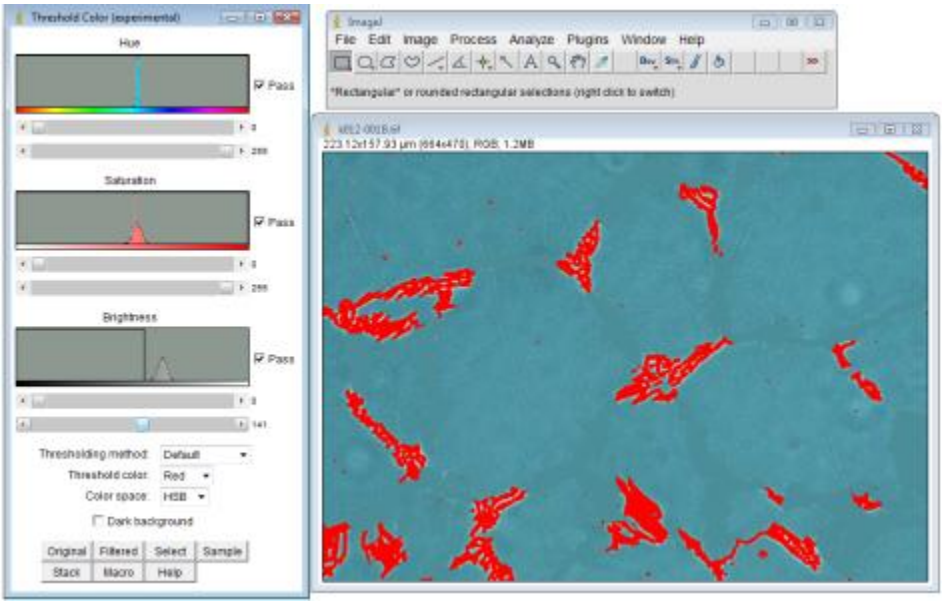

Figure 3.6: Particle regions threshold for the first layer of sample K0; $Cr_{23}C_{6.}$

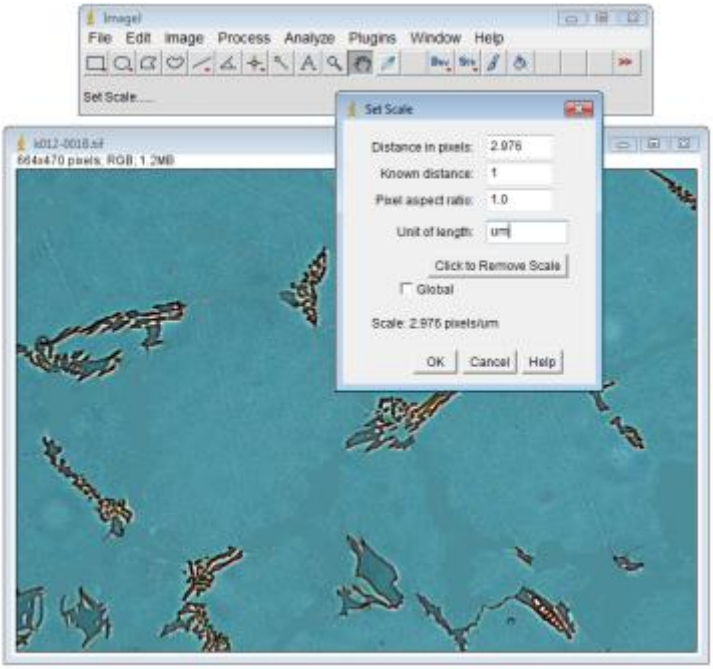

Figure 3.7: Re-scaling the measurement unit from pixels into µm.

3.6.2 Area measurement

Using analyze tool of NIH ImageJ, the analyze particle command has been selected to counts and measure the area of threshold image. Figure 3.8 shows the command windows of the process. The analysis was done by scanning the selected particle within the range of threshold. The result obtained was presented in unit of μm^2.

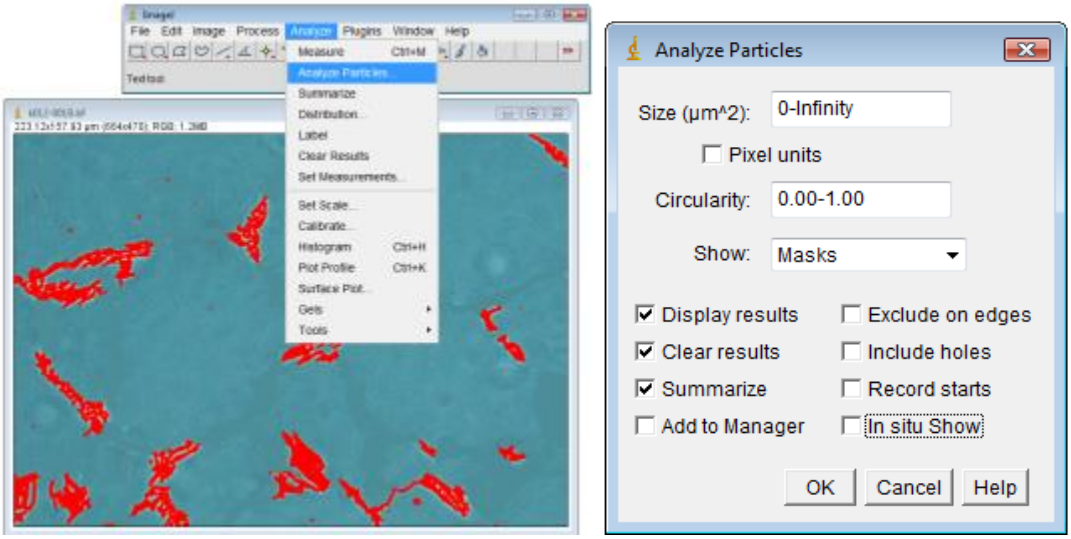

Figure 3.8: Command to analyze particles threshold.

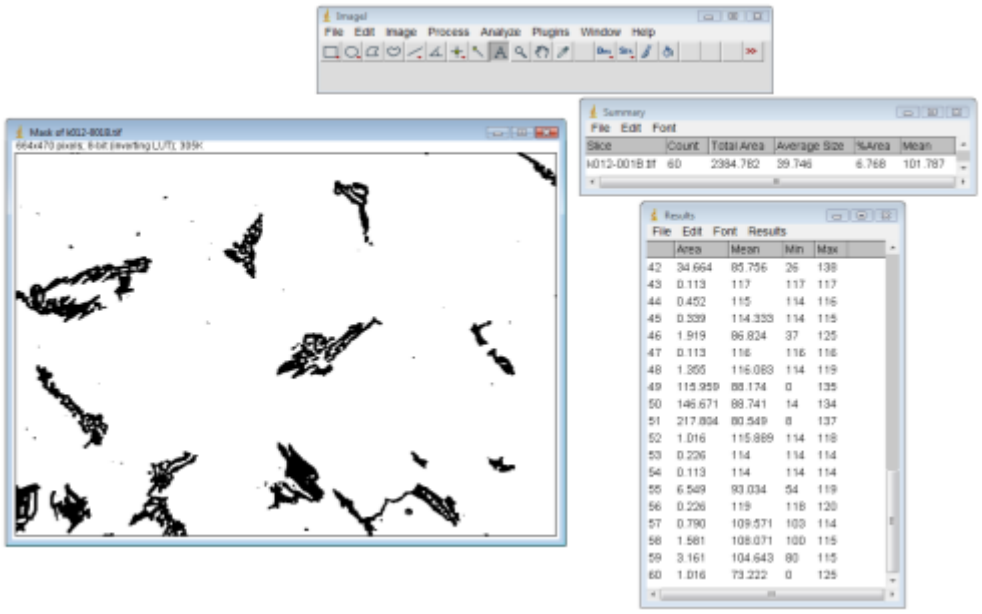

Figure 3.9: Result presentation of analyzed particle threshold; masks of particles, table of results, and result summary.

Figure 3.9 above shows the masks, results and summary of the analysis as requested. The summary window presented the counts, total area, average size, percentage and mean area of the analyzed particles. Each of the images would produce their own measurement information. Later, the collection of information was tabulated in the Microsoft Excel spreadsheet. The mean area calculated was then multiplied with the number of stacking images in which each layer equals to 0.5µm depth.

$$\textit{Mean Area Sample} = \frac{\textit{Total Area of precipitate in 50 layers}}{\textit{50 layers}} \quad (6)$$

$$\textit{Mean Volume of sample} = \textit{Mean Area Sample x 50 x 0.5 µm} \quad (7)$$

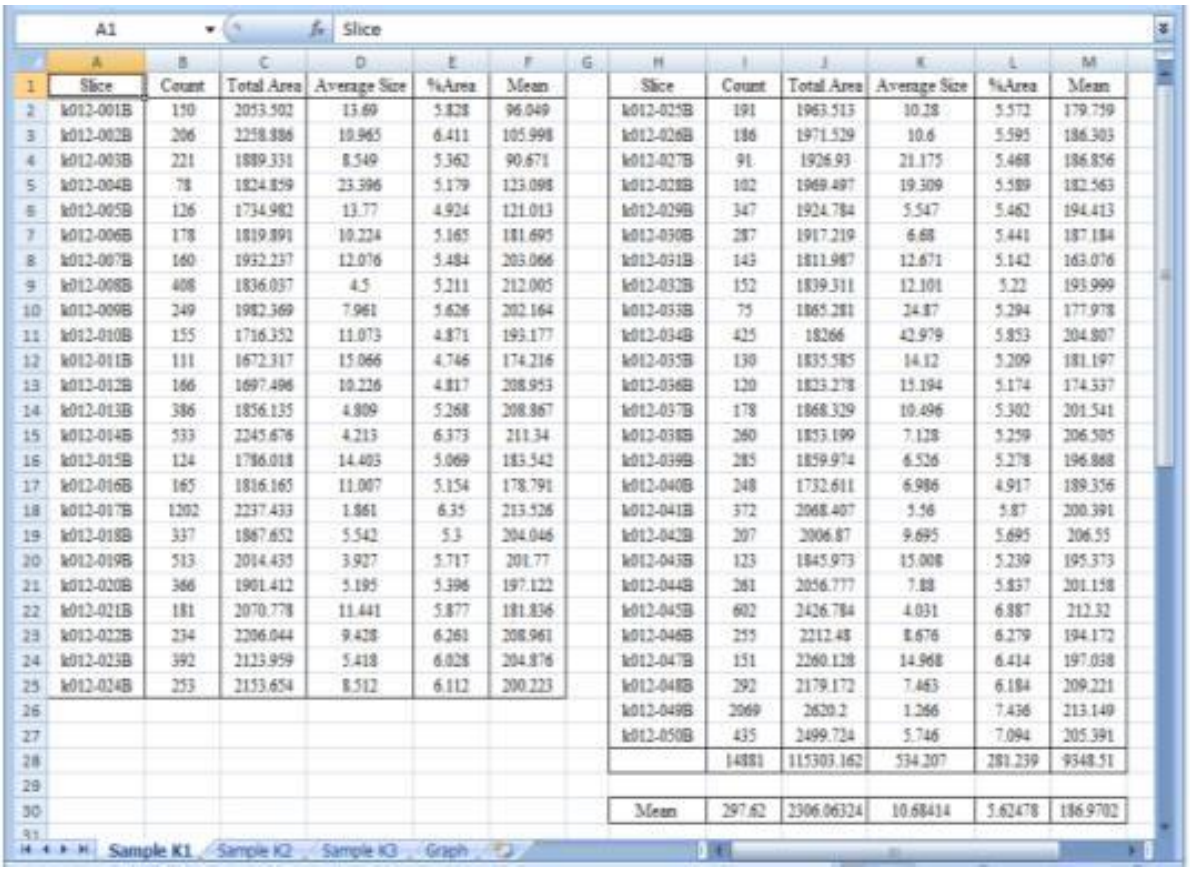

Slice	Count	Total Area	Average Size	%Area	Mean
k012-001B	150	2053.502	13.69	5.828	96.049
k012-002B	206	2258.886	10.965	6.411	105.998
k012-003B	221	1889.331	8.549	5.362	90.671
k012-004B	78	1824.859	23.396	5.179	123.098
k012-005B	126	1734.982	13.77	4.924	121.013
k012-006B	178	1819.891	10.224	5.165	181.695
k012-007B	160	1932.237	12.076	5.484	203.066
k012-008B	408	1836.037	4.5	5.211	212.005
k012-009B	249	1982.369	7.961	5.626	202.164
k012-010B	155	1716.352	11.073	4.871	193.177
k012-011B	111	1672.317	15.066	4.746	174.216
k012-012B	166	1697.496	10.226	4.817	208.953
k012-013B	386	1856.135	4.809	5.268	208.867
k012-014B	533	2245.676	4.213	6.373	211.34
k012-015B	124	1786.018	14.403	5.069	183.542
k012-016B	165	1816.165	11.007	5.154	178.791
k012-017B	1202	2237.433	1.861	6.35	213.526
k012-018B	337	1867.652	5.542	5.3	204.046
k012-019B	513	2014.435	3.927	5.717	201.77
k012-020B	366	1901.412	5.195	5.396	197.122
k012-021B	181	2070.778	11.441	5.877	181.836
k012-022B	234	2206.044	9.428	6.261	208.961
k012-023B	392	2123.959	5.418	6.028	204.876
k012-024B	253	2153.654	8.512	6.112	200.223

Slice	Count	Total Area	Average Size	%Area	Mean
k012-025B	191	1963.513	10.28	5.572	179.759
k012-026B	186	1971.529	10.6	5.595	186.303
k012-027B	91	1926.93	21.175	5.468	186.856
k012-028B	102	1969.497	19.309	5.589	182.563
k012-029B	347	1924.784	5.547	5.462	194.413
k012-030B	287	1917.219	6.68	5.441	187.184
k012-031B	149	1811.987	12.671	5.142	163.076
k012-032B	152	1839.311	12.101	5.22	193.999
k012-033B	75	1865.281	24.87	5.294	177.978
k012-034B	425	18266	42.979	5.853	204.807
k012-035B	130	1835.585	14.12	5.209	181.197
k012-036B	120	1823.278	15.194	5.174	174.337
k012-037B	178	1868.329	10.496	5.302	201.541
k012-038B	260	1853.199	7.128	5.259	206.505
k012-039B	285	1859.974	6.526	5.278	196.868
k012-040B	248	1732.611	6.986	4.917	189.356
k012-041B	372	2068.407	5.56	5.87	200.391
k012-042B	207	2006.87	9.695	5.695	206.55
k012-043B	123	1845.973	15.008	5.239	195.373
k012-044B	261	2056.777	7.88	5.837	201.158
k012-045B	602	2426.784	4.031	6.887	212.32
k012-046B	255	2212.48	8.676	6.279	194.172
k012-047B	151	2260.128	14.968	6.414	197.038
k012-048B	292	2179.172	7.463	6.184	209.221
k012-049B	2069	2620.2	1.266	7.436	213.149
k012-050B	435	2499.724	5.746	7.094	205.391
	14881	115303.162	534.207	281.239	9348.51
Mean	297.62	2306.06324	10.68414	5.62478	186.9702

Figure 3.10: Microsoft Excel spreadsheet used to tabulate the entire stacks of analyzed particles.

3.6.3 Three Dimensional (3D) reconstruction and visualization

To reconstruct and visualize the three dimensional (3D) of stack images, all the masked images were re-stacked and were saved into a new TIFF image file before it is to perform the reconstruction function. Then 3D Plug-in was used to generate Volume Viewer (See Figure 3.11). The volume viewer windows would pop out as in

Figure 3.12. In this project, the volume has been processed in slow resolution and is presented in isometric view.

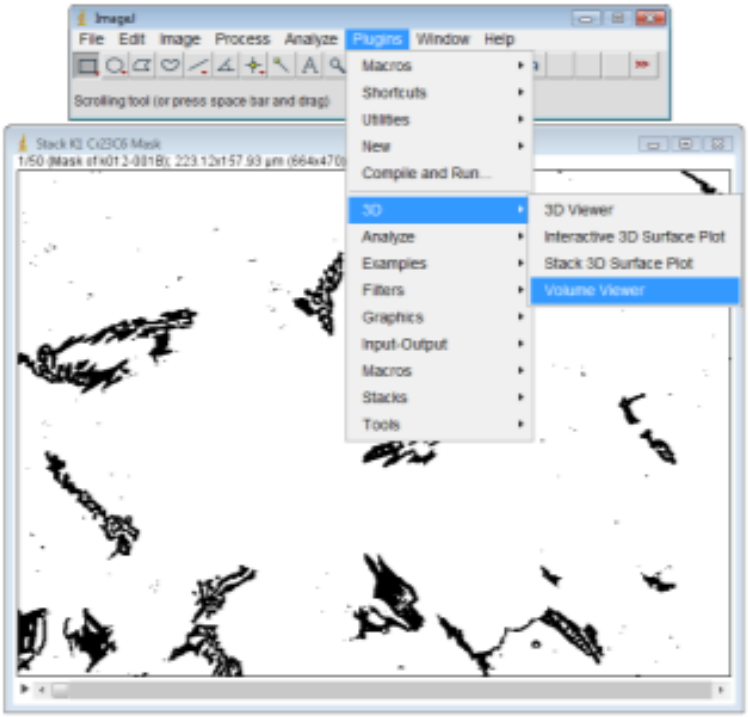

Figure 3.11: The masks images of sample K0 were re-stacked and saved in different TIFF file.

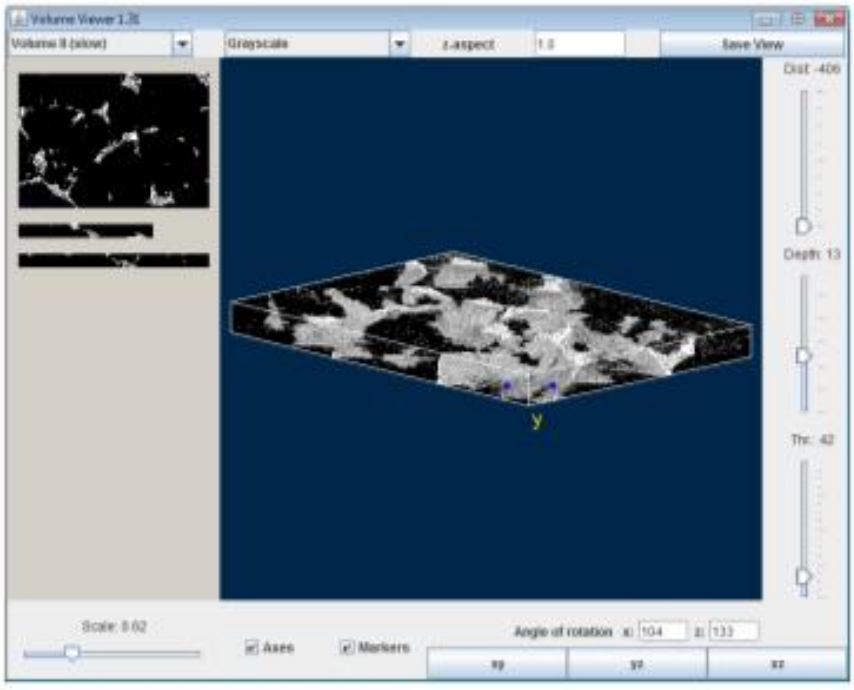

Figure 3.12: The volume viewer showing the distributions of $Cr_{23}C_6$ of sample K1 in isometric view.

CHAPTER 4

RESULTS AND DISCUSSION

4.1 Results

The image analysis has provided significant quantitative analyses of the carbide precipitates formation in the reformer tube. The influence of service temperature and pressure to the carbide precipitation has been observed and presented in tables and graphs to relate between the service conditions and the carbide precipitates characteristics. Various literature sources have been reviewed to discuss the findings and to formulate a conclusion.

4.2 Effect of different service condition on the carbide precipitation formation.

Table 4.1 below shows the tabulated data for the variation of service temperature and service pressure exposure and their relation to the average particle size of precipitates formed.

Table 4.1: Data tabulation of average particle size to the service temperature.

Sample	Service Temperature (°C)	Mean Volume (10^3 µm^3)		
		$Cr_{23}C_6$	NbC	TiC
K0	N/A	57.652	21.762	0.00
K1	888	87.992	29.719	5.778
K2	886	74.911	26.732	1.956
K3	848	73.799	25.032	0.067

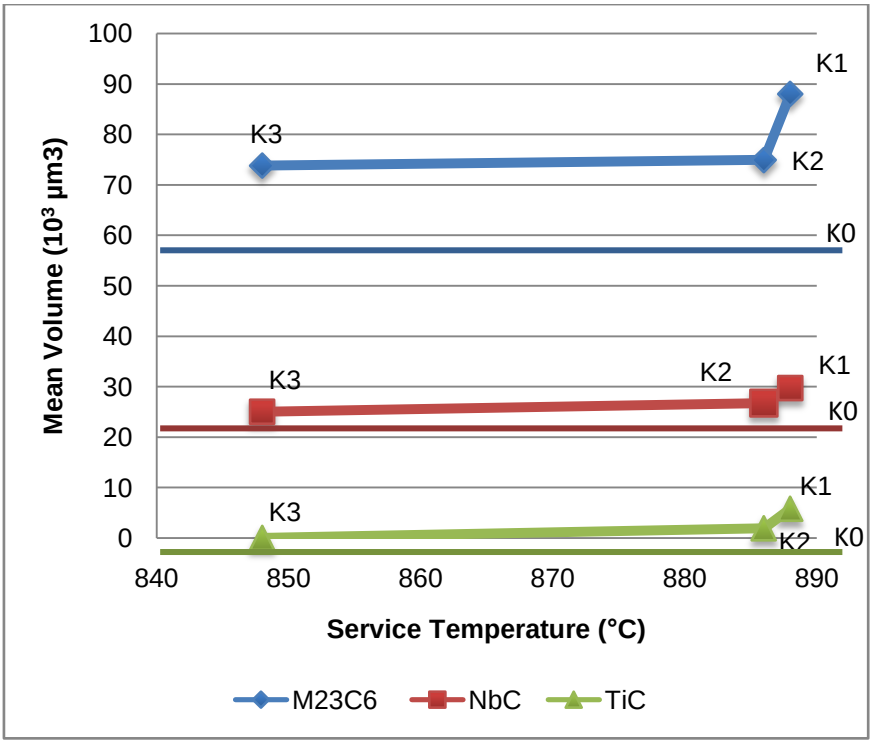

Figure 4.1: Graph of mean volume of precipitate against the service temperature.

As shown in Figure 4.1, the mean volume of chromium carbide, $Cr_{23}C_6$ precipitates is increasing as the service temperature increase. At 888 ºC, the service temperature of Sample K1, the mean volume of chromium carbide precipitates is the largest compared to the other lower temperature samples. Figure 4.2 shows large chromium carbide precipitates that formed at the grain boundaries. However, at certain higher temperatures, secondary precipitation is expected to happen in which it can be seen clearly as a dispersion of fine particles within austenitic matrix [2]. In sample K1, there is little presence of secondary precipitates that it is likely because of chromium depletion and outward diffusion related to the development of chromium-rich oxide layer [2]. During the degradation, the carbides detached away from the grain boundaries. Isolated voids were also apparent presumably due to Kirkendall effect. Kirkendall effect describes the phenomenon when two solids diffuse into each other at different rates. The atoms of the solids don't change places directly; rather diffusion occurs where voids are left opened [18].

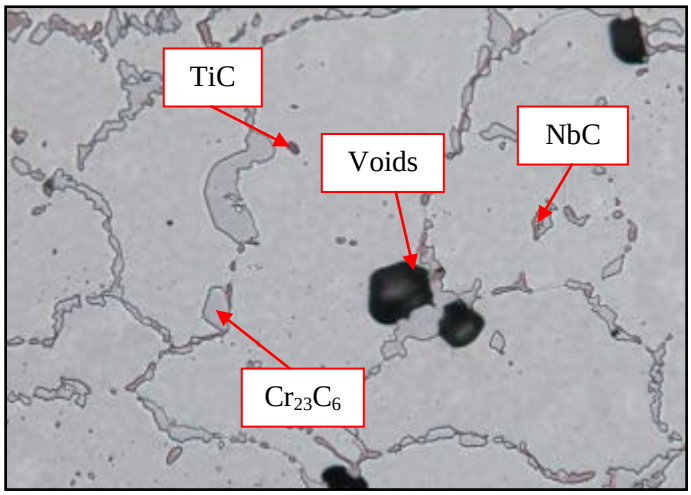

Figure 4.2: Optical image of Sample K1 at 200X magnification.

At service temperature of sample K2, 886ºC the mean volume of $Cr_{23}C_6$ precipitates, abruptly becomes smaller than in K1 sample. It is believed that this is caused by the precipitation of fine secondary carbide. As can be seen in Figure 4.3, an optical image of sample K2 shows that there is presence of fine precipitates away from the grain boundary labeled as secondary precipitates. While at lower temperature of 848 ºC, massive precipitation of fine secondary precipitates has caused the remaining mean volume of primary precipitates become smaller as presented in Figure 4.4.

As have been mentioned in section 3.5 previously, during highlighting the features of carbide precipitates, only the large and significant primary carbides were selected. The large carbide precipitates is likely to have formed during the early stage of precipitation. Therefore, the increase in temperatures in sample K2 and K3 is the reason chromium carbide precipitates were detected less in the microstructure. At 886ºC, the secondary precipitates occur but at lower amount compared to 848ºC as shown in Figure 4.4.

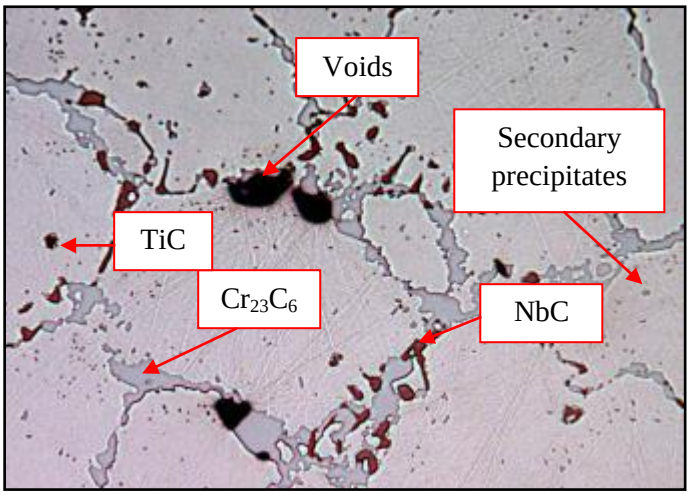

Figure 4.3: Optical image of Sample K2 at 200X magnification.

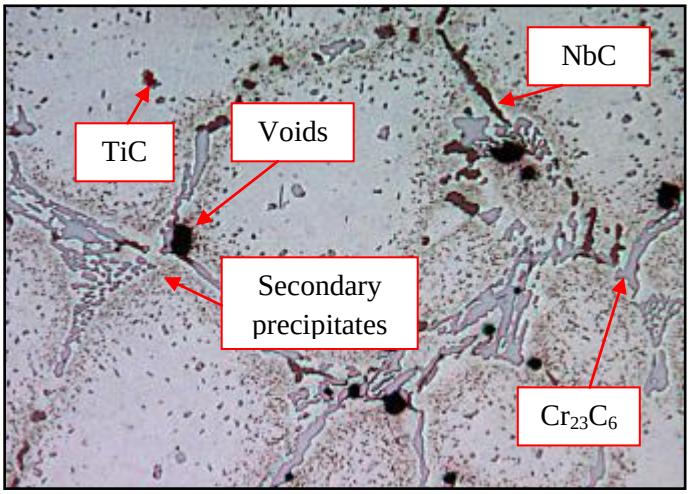

Figure 4.4: Optical image of Sample K3 at 200X magnification.

It has been reported that NbC precipitates is not stable in the range of temperature between 700 and 900 ºC. From Figure 4.1, at 888 ºC the niobium carbide precipitates were slightly bigger than at 848ºC and 886ºC, it may due to the vacancy diffusion of niobium elements to the carbon elements during chromium depletion to form secondary precipitates or is there any case of chromium oxide formation. At higher temperature of 888ºC or even at 886ºC, niobium carbide is unstable, and there is possibility to transform into a nickel-niobium silicide, $Nb_6Ni_{16}Si_7$ which some study regarded it as G-phase [2]. However, the G-phase could best be identified by using X-ray diffraction spectra and are not easily detected by observation through optical images.

Titanium carbide precipitates are larger at 888ºC temperature compared to at service temperature of 848ºC and 886ºC. The coarsening rate varies with the composition in material with TiC. If there is a presence of Cr and Ni, the coarsening will become slightly faster. This is because Ni is a strong austenite stabilizer. A study also proved that the coarsening rate increases with increasing temperature [19]. This effect is caused both by increase in the diffusion rates and the increase in solubility of the Titanium element in the matrix. However, the slight decrease of the Titanium carbide average size at 886ºC is may due to the formation of intermetallic phase rich in silicon, nickel, titanium that is very likely to be the G phase denoted as $M_6Ni_{16}Si_7$ [20].

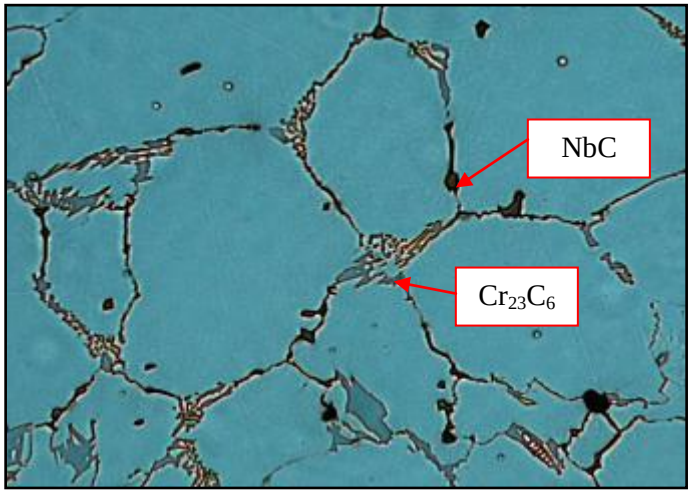

Figure 4.5: Optical image of Sample K0 at 200X magnification.

The microstructure of the as-cast sample which is sample K0 consisted of an austenitic matrix and a network of two types of primary carbides which are chromium and niobium as shown in Figure 4.5. No titanium carbides formation has occurred. The shapes of primary carbides are finer compared to the ex-serviced samples as in K1, K2, and K3 where the primary carbides coarsen with increase in servicing temperature [3]. This is the reason the mean volume of carbide precipitates are always the lowest in the as-cast sample.

4.3 Service Temperature of the sample XH and XC.

The prediction of two unknown samples XC and XH will be made based on the size comparison of all three precipitates - Chromium Carbide, Niobium Carbide and Titanium Carbide, and comparing them to the data for K1, K2, and K3 samples. To make the comparisons more reliable, the data has been plotted into regression model as presented in Figure 4.6, 4.7, and 4.8.

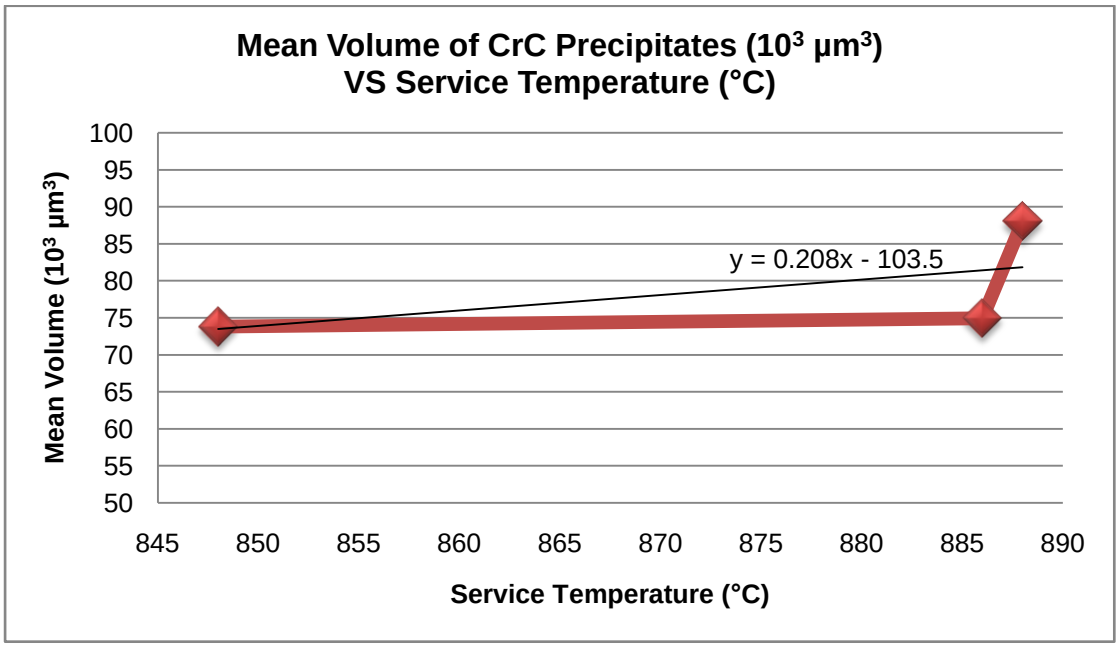

Figure 4.6: The mean volume of Chromium Carbide precipitates against the service temperature.

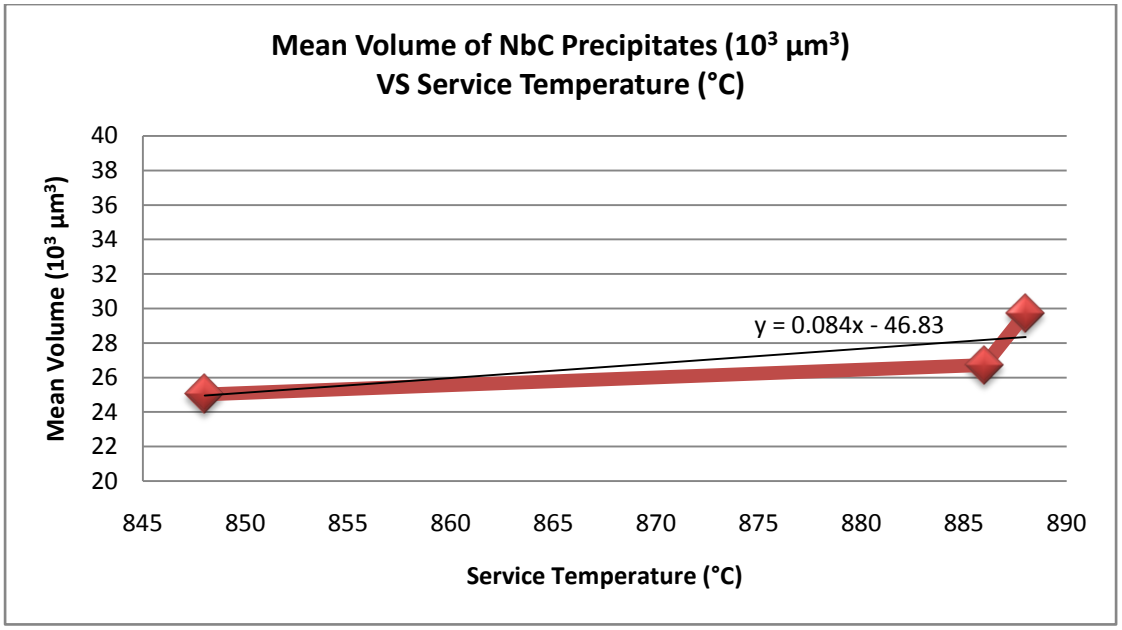

Figure 4.7: The mean volume of Niobium Carbide precipitates against the service temperature.

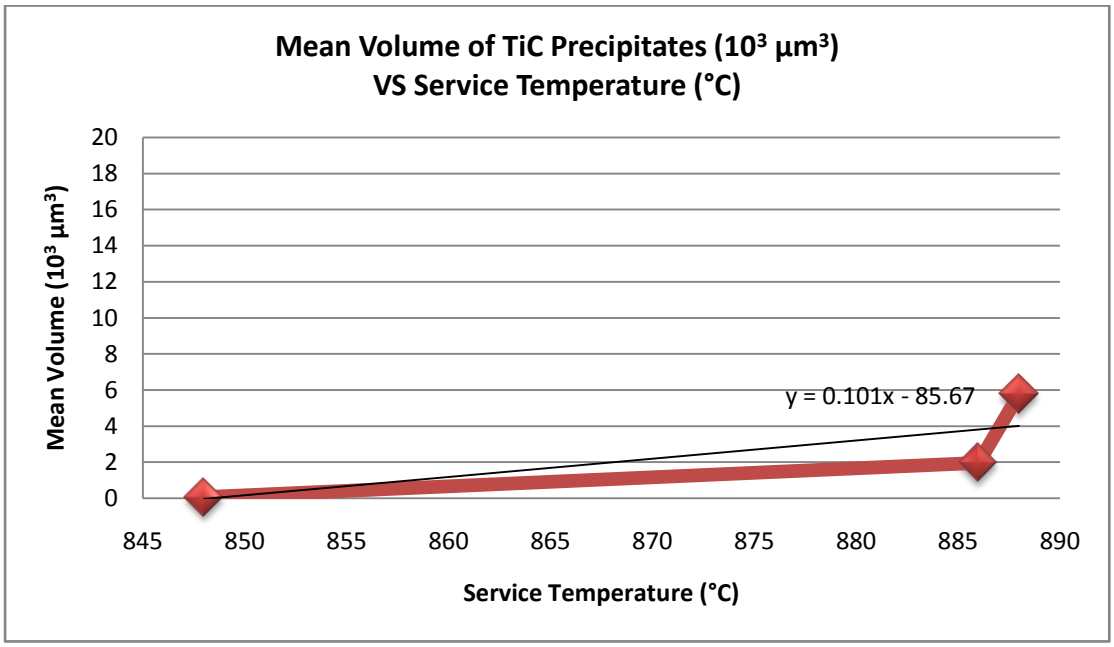

Figure 4.8: The mean volume of Titanium Carbide precipitates against the service temperature.

Sample XH and XC mean volume has been analyzed and the findings are as below:

Table 4.2: XH and XC tabulated data.

Sample	Service Temperature (ºC)	Mean Volume (10^3 µm^3)		
		$Cr_{23}C_6$	NbC	TiC
XH	Unknown (Overheat)	90.70	18.40	0.26
XC	Unknown (Normal)	73.20	24.10	3.70

From the linear equations obtained from the respective graphs, the predicted temperatures are as follows.

Table 4.3: Table for calculated temperature based on linear equations produced in graphs.

Sample	Service Temperature (ºC)	Predicted Temperature Based on Precipitate Formation (ºC)		
		$Cr_{23}C_6$	NbC	TiC
XH	Unknown (Overheat)	933.7	776.6	850.8
XC	Unknown (Normal)	849.5	844.4	884.9

All the calculated data are then presented in correlation and regression models to study the strongest linear relationship between the two variables, which is the mean volume of precipitates, and the operating temperature. The regression coefficient should be closer to 1.0 or -1.0 as indication of stronger relation between the variables [20]. Also, graphically, the closer the points are to the straight line, the stronger the linear relationship between the two variables.

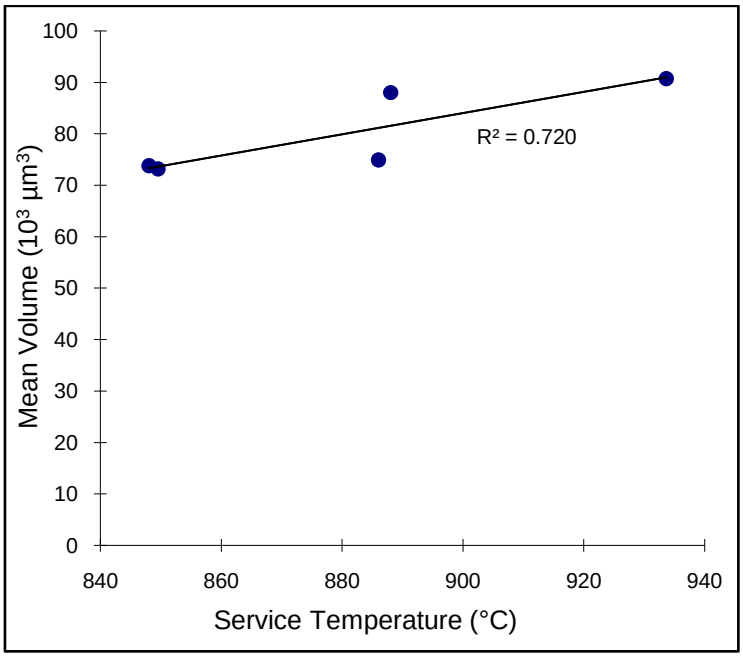

Figure 4.9: The linear regression of mean volume of $Cr_{23}C_6$ with the operating temperature.

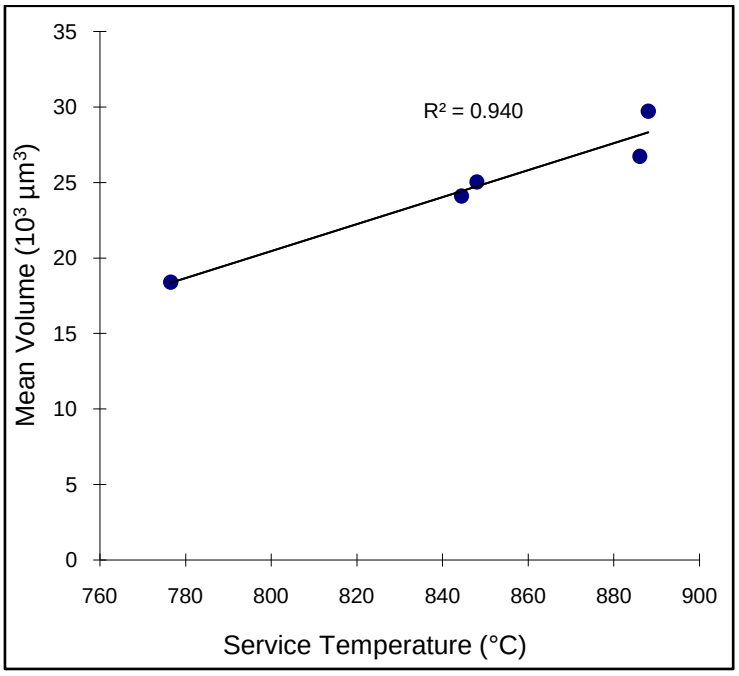

Figure 4.10: The linear regression of mean volume of NbC with the service temperature.

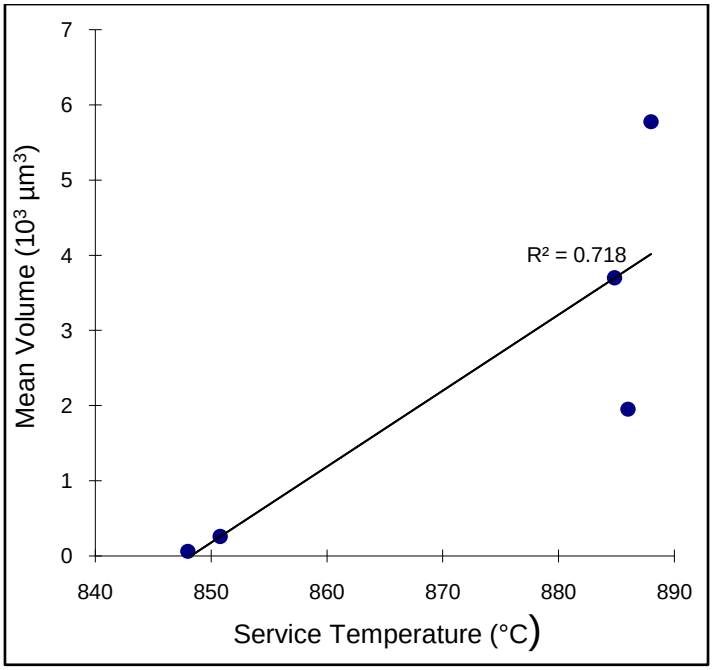

Figure 4.11: The linear regression of mean volume of TiC with the service temperature.

From the graphs plotted, it is observed that the regression coefficient for mean volume of NbC precipitates has the closer value to 1 while for $Cr_{23}C_6$ precipitate graph is the second closest. However, the calculation presented in Table 4.3 shows that the temperature for XH sample, 993.7ºC calculated from the graph in Figure 4.6 fit the overheating condition of reformer tubes, which is more than 900ºC. Also the temperatures calculated for XC, which is 849.2ºC, are in within the range of 850–900ºC, which can be considered normal operating temperature. Furthermore, the NbC and TiC precipitate sizes for the unknown sample did not follow the same trend as in the ex-service samples. It is believed that the significant overheating of sample XH resulted in the transformation of NbC and TiC precipitates into perhaps G-phase, which would then explain the reduction in sizes for the NbC and TiC particles. Therefore, from the study, the best predicted temperature for XH and XC samples are 993.7ºC and 849.2ºC respectively which are obtained from the mean volume of $Cr_{23}C_6$ precipitates in relation to the service temperature.

CHAPTER 5

CONCLUSION AND RECOMMENDATION

5.1 Conclusion

From this project, it can be concluded that the results of carbide precipitation characterization of steam-methane reformer tube are greatly influenced by the service conditions. Service temperature has the major influence to the reformer tube since for the reaction to occur; it requires a very high operating temperature.

The findings in this project show that a slight change in temperature would change the behavior of precipitates. The increase and decrease in size of precipitates are due to the heating affect that would allow primary precipitate to transform into secondary precipitate. At relatively higher temperature, the carbides even can transform into other potential compounds such as metal oxide due to servicing environment with presence of water and oxygen. Metal oxides generally formed at the outer layer of the reformer tubes. In this case, chromium is more likely to form chromium-rich oxide. The transformation of carbides into other compounds would cause degradation. Also Titanium and Niobium rich carbides are potentially transforming into G-phase, a formation with Nickel and Silicon that are present in the alloy. It is generally induced by the ageing of the reformer tubes themselves.

The service temperature experienced by the unknown condition of the samples also can be predicted. The mean volume of precipitates measured at their specific service temperature has provided appropriate linear relationship between the two variables to estimate the temperature of the unknown samples. To make the prediction become more reliable, a linear regression model has been applied to compare the strength between the two variables, mean volume of precipitates with the service temperature. Based on the characteristics of the chromium carbide particles with respect to service

temperature, it was determined that the overheated sample experienced a temperature of 993.7ºC which was much higher than the intended service temperature.

Above all, the whole project would not be successful without proper image processing. All the findings greatly depend on the integrity of the data samples, the image processing works and image analysis. Image analysis is the backbone of microstructure characterization. In this project, the image of carbide precipitates has been selected according to the types and their volume were measured through 50 layers. The reason to take many layers are to obtain as accurate measurement as possible since, the precipitates are changing in shapes and sizes along the depth. The accuracy of the results obtained is greatly depending on how the image analysis has gone through.

5.2 Recommendations

There are two major recommendations to improve the project findings. Firstly, image analysis is the crucial part to obtain the most promising result. Part of image analysis which is image processing should be done in details and to be avoided in making mistakes. During selecting the carbide precipitates, confirmation of the precipitates with EDX or other techniques can remove any ambiguities. Improved image pre-processing using reliable image processing software to remove unwanted blemishes or marks on the micrographs could also give better results. Apart from that, to improve the findings, more samples should be added in order to get a good data comparison.

REFERENCES

[1] M. De Jonga, A.H.M.E. Reindersa, J.B.W. Kokb, G.Westendorpc, *Optimizing a steam-methane reformer for hydrogen Production*, International Journal of Hydrogen Energy 2009 ; 34 : 285 – 292.

[2] A. Alvino, D. Lega, F. Giacobbe, V. Mazzocchi, A. Rinaldi, *Damage characterization in two reformer heater tubes after nearly 10 years of service at different operative and maintenance conditions*, Engineering Failure Analysis, 2010;17: 1526–1541.

[3] A.W. Azmi, "*Three-dimensional analysis of creep void formation in steam-methane reformer tubes"*, doctoral dissertation, Dept. Mechanical Engineering, University of Canterbury, 2007.

[4] J.H. Lee, W.J. Yang, W.D Yoo, K.S Cho, *Microstructural and mechanical property changes in HK40 reformer tubes after long term use*, Engineering Failure Analysis, 2009;16:1883–1888.

[5] K.R. Ashok, K.S. Samarendra, N.T. Yogendra, S. Jagannathan, D. Gautam, C. Satyabrata, S. Raghubir, *Analysis of failed reformer tubes*, National Metallurgical Laboratory (CSIR) 2002.

[6] Le May, T.L. DaSilveirab, C.H. Viannac, *Criteria for the evaluation of damage and remaining life in reformer furnace tubes*, ht. J. Pres. Ves. & Piping,1996; 66:233-241.

[7] T.L DaSilveira., I.L. May, *Reformer furnaces: materials, damage mechanisms, and assessment*,The Arabian Journal for Science and Engineering, Volume 31, Number 2C.

[8] J. Huber, D. Jakobi, *Centricast Materials for High-Temperature Service*, International Conference & Exhibition + Syngas, 2011.

[9] M. De Mattos, V.M Souza, S. Martin, *Supported Nickel Catalysts for Steam Reforming of Methane*, 2ndMercosur Congress on Chemical Engineering, 4thMercosur Congress on Process Systems Engineering, ENPROMER, 2005.

[10] P.V Beurden, *The Catalytic Aspects of Steam-Methane Reforming*, A Literature Survey, ECN, 2004.

[11] S.G Kang, R.S. Sung, D.K. Sang, S.K. Kyoung, S.P Chu, *Hydrogen production from two-step steam methane reforming in a fluidized bed reactor*, Korea Advanced Institute of Science and Technology (KAIST), 2008.

[12] F. Gallucci *et al.*, *Experimental Study of the Methane Steam Reforming Reaction in a Dense Pd/Ag Membrane Reactor*, Ind. Eng. Chem. Res. 2004; 43: 928.

[13] L.H. De Almeida, A.F. Ribeiro, I.L. May, *Microstructural characterization of modified 25Cr – 35Ni centrifugally cast steel furnace tubes*, Materials Characterization 2003;49: 219-229.

[14] P. Bogdan, *Effect of Nb and Ti additions on microstructure, and identification of precipitates in stabilized Ni-Cr cast austenitic steels*, Materials Characterization, 2001;47:181-186.

[15] G.F.V. Voort, H.M. James, J.R. Davis, J.D. Destafani, D.A. Dietrich, G.M. Crankovic, M.J. Frissel (Eds.), ASM Handbook: Metallography and Microstructures, Vol. 9, ASM International, USA, 2004.

[16] Research Services Branch. Available: http://rsb.info.nih.gov/ij/.

[17] Schmidt + Clemens, G/CA 4852 Micro Material Data Sheet, 2001.

[18] N. Hideo, *The Discovery and Acceptance of the Kirkendall Effect: The Result of a Short Research Career*, (the journal) JOM, 49 (6) (1997), pp. 15-19.

[19] A. Gustafson, *Coarsening of TiC in austenitic stainless steel – experiements and simulations in comparison*, Materials Science and Engineering A287 (2000) 52 – 58.

[20] B. Piekarski, *Effect of Nb and Ti additions on microstructure, and identification of precipitates in stabilized Ni-Cr cast austenitic steels,* Materials Characterization 47 (2001) 181 -186.

[21] A. Choudhury. (2010). Correlation and Regression.*Explorable.* Available: http://explorable.com/correlation-and-regression.html